



ELSEVIER

Contents lists available at ScienceDirect

## Deep-Sea Research II

journal homepage: [www.elsevier.com/locate/dsr2](http://www.elsevier.com/locate/dsr2)

## The cold-core eddy and strong upwelling off the coast of New South Wales in early 2007

Peter R. Oke\*, David A. Griffin

Centre for Australian Weather and Climate Research: a partnership between CSIRO and the Bureau of Meteorology; and Wealth from Oceans National Research Flagship, Australia

## ARTICLE INFO

## Article history:

Received 15 June 2010

Accepted 15 June 2010

Available online 1 July 2010

## Keywords:

East Australian Current

Ocean Reanalysis

Upwelling

Eddy

## ABSTRACT

During the Austral summer of 2006–07 a series of extreme oceanic events occurred in the Tasman Sea. Following a series of strong wind-driven upwelling events, an intense cold-core eddy developed off Sydney, Australia. A data-assimilating, eddy-resolving ocean model is used to create a three-dimensional time-varying reanalysis of these events. The reanalysis indicates that the cold anomalies associated with the upwellings were in excess of  $-5\text{ }^{\circ}\text{C}$  near the coast, where sea level decreased by as much as 0.2 m. The reanalysed three-dimensional structure of the cold-core eddy shows the eddy "leaning" to the west–north–west, in towards the continental shelf. The diameter of the eddy is about 100 km and the sea-level anomaly at the eddy centre peaks at around  $-1\text{ m}$ , with an associated sub-surface temperature anomaly in excess of  $-8\text{ }^{\circ}\text{C}$  at 200 m depth, corresponding to an upward isotherm excursion of 600 m. The circulation around the cyclonic eddy is ageostrophic, with upwelling in the southern sector of the eddy (where flow is onshore and climbing the continental slope) and downwelling in the northern sector (where flow is descending off the slope). Three-dimensional trajectories of water parcels around the eddy involve 50–100-m vertical excursions. Based on the reanalysed circulation and composite satellite images of Chlorophyll-a, we hypothesise that the circulation around the eddy led to significant nutrient enrichment in the euphotic zone around the perimeter of the eddy.

© 2010 Elsevier Ltd. All rights reserved.

### 1. Introduction

During the Austral summer of 2006–07 two remarkable oceanic events occurred in the Tasman Sea. Firstly, there was a series of strong, sustained, upwelling-favourable wind events that resulted in unseasonably cold coastal waters along much of the New South Wales coast. Secondly, a very intense cold-core eddy developed at  $33.5^{\circ}\text{S}$  at the foot of the continental rise just off Sydney ( $34^{\circ}\text{S}$ ), with sea-level anomalies (SLAs) of almost 1 m below mean sea level at its core and cold temperature (T) anomalies exceeding  $-8\text{ }^{\circ}\text{C}$  at 200 m depth. The intensity of these events was so great that explanations were demanded by Australian news sources. Coincident with these events, satellite observations show very high levels of Chlorophyll-a (Chl-a) along the coast; and above-average levels of Chl-a offshore. Based on results from a data assimilating, eddy-resolving ocean general circulation model, we describe the three-dimensional circulation associated with these events; and propose a mechanism for the nutrient enrichment of surface waters around the cyclonic eddy.

\* Corresponding author. Tel.: +61 3623 25387.  
E-mail address: [peter.oke@csiro.au](mailto:peter.oke@csiro.au) (P.R. Oke).

The salient oceanographic feature of the waters off the New South Wales coast is the East Australian Current (EAC) and the associated mesoscale eddy field (Fig. 1). These waters are generally low in nutrients, a characteristic of their source waters in the Coral Sea, and the wind stress is also predominantly downwelling favourable (southerly), so any sub-surface nutrients are rarely upwelled to the euphotic zone. Despite this, nutrient enrichment and algal blooms do occur in response to occasional upwelling-favourable wind events, encroachment of the EAC, or its eddies, onto the continental shelf, or the separation of EAC from the shelf (Blackburn and Cresswell, 1993; Tranter et al., 1986; Hallegraef and Jeffrey, 1993; Cresswell, 1994; Gibbs et al., 1997; Oke and Middleton, 2000; Ajani et al., 2001; Roughan and Middleton, 2002; Ridgway and Dunn, 2003; Baird et al., 2007; MacDonald et al., 2009). As a result of the episodic nature of these events concentrations of Chl-a are typically low in the Tasman Sea.

The purpose of this paper is to provide a synoptic description of the ocean circulation off the New South Wales coast between December 2006 and April 2007, when the above-mentioned upwellings and eddy formation occurred, in order to better understand the factors that may have contributed to these extreme events. To these ends, we present an analysis of the mesoscale ocean circulation for this period using results from the

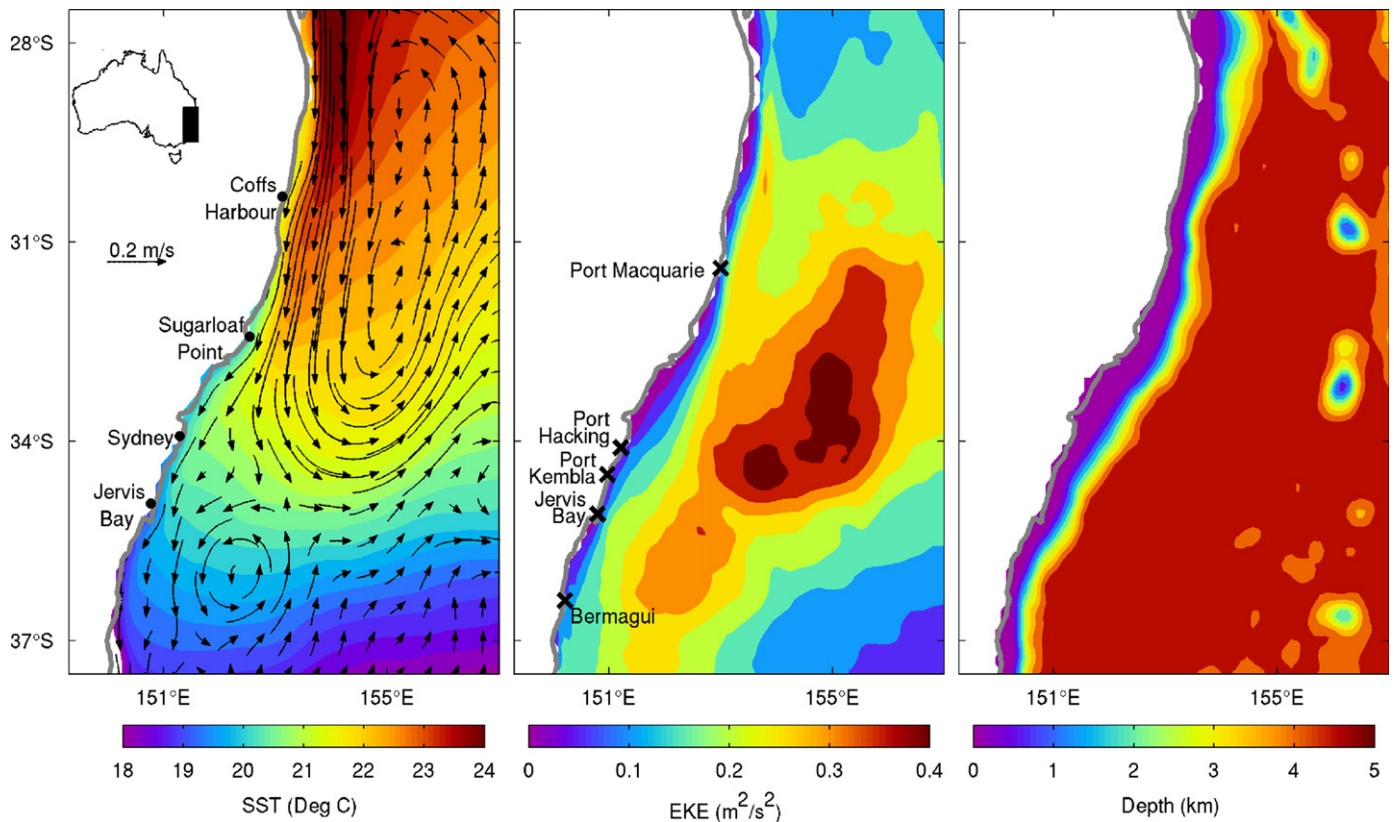


**Fig. 1.** Thirteen-year average (1993–2006) SST and surface velocities (left), eddy-kinetic energy (EKE; middle) computed from daily mean fields of surface velocity, from BRAN2p1, and model topography (right). The inset on the left panel shows the location of the region of interest off south eastern Australia. The crosses on the middle panel denote tide gauge locations referred to in Fig. 3.

Bluelink ReANalysis (BRAN) system (Oke et al., 2005, 2008; Schiller et al., 2008). Briefly, BRAN involves the integration of a global ocean model that is eddy-resolving around Australia and the sequential assimilation of altimeter, sea-surface temperature (SST) and in situ Argo temperature (T) and salinity (S) observations. Despite the regional focus, the assimilation is performed globally, using all available observations.

## 2. Reanalysis system

The Bluelink ReANalysis (BRAN) system that is used here is comprised of a global ocean general circulation model, called the Ocean Forecasting Australia Model (Schiller et al., 2008), and an ensemble data assimilation system, called the Bluelink Ocean Data Assimilation System (Oke et al., 2008). The Bluelink system is run operationally at the Bureau of Meteorology for the production of forecasts (Brassington et al., 2007) and has been used for several scientific studies (Oke et al. 2005, 2008, 2009; Oke and Schiller, 2007; Schiller et al., 2008, 2009, 2010).

The Bluelink ocean model is a configuration of the Modular Ocean Model (Griffies et al., 2004; version 4.0d). The model grid has 10 m vertical grid spacings over the top 200 m, and 1/10° horizontal grid spacing in the 90°-sector centred on Australia and south of 16°N. This translates to zonal and meridional resolution of about 11 km and 9–10 km (at 26–36°S), respectively. The horizontal grid spacing is 0.9° across the Indian and Pacific Ocean and 2° in the Atlantic Ocean. To accommodate the inhomogeneous resolution, the horizontal viscosity is resolution- and state-dependent, based on the Smagorinsky-scheme (Griffies and Hallberg, 2000). The bottom topography was constructed from a

range of different sources, as documented by Schiller et al. (2008). The turbulence closure model used here is a version of the hybrid mixed-layer scheme described by Chen et al. (1994). For long model runs, such as free spin-up runs and BRAN experiments, the model is forced by 6-hourly heat, freshwater and momentum fluxes from ECMWF, using fields from ERA-40 (Kallberg et al., 2004) for the period prior to August 2002, and 6-hourly operational forecasts thereafter.

The Bluelink assimilation system uses an Ensemble Optimal Interpolation (EnOI) scheme that draws on a 120-member ensemble of intraseasonal model anomalies. The ensemble is generated from a long non-assimilating integration of the model. The ensemble is stationary in time, acting as a time-invariant database that is intended to define the sub-space of the ocean model. Using ensemble data assimilation techniques (see Oke et al., 2008), the model-observation misfits (the background innovations) are projected onto the model sub-space, to compute an increment, or correction, to a model background field during each weekly assimilation cycle. Thus, the assimilation system is multi-variate, using the statistics of the ensemble to interpolate and extrapolate model-observation misfits onto the full-model grid, and for all model variables. So for example, an observation of one variable, say temperature, is compared to the model background field, and the difference is projected onto the model state, using the ensemble, yielding an increment not just for temperature, but also salinity, velocity, and sea level. In practice, many observations of different types are assimilated simultaneously at each assimilation step. In this case, the assimilation system solves an analysis equation, using explicit estimates of the observation errors to weight their relative impact, together with the ensemble statistics, to compute a weighted least-squares analysis that

combines the available observations with the model-generated background field. The details of Bluelink Ocean Data Assimilation System are described by Oke et al. (2005, 2008).

For the BRAN experiment used here, an analysis is computed every seven days. During each assimilation step an analysis and analysis increment is computed for temperature, salinity, sea-level, and horizontal velocity, by combining a daily mean model field with observations of along-track SLA, AMSR-E SST, and Argo T/S. The analysis increments are then applied to the model over a 12-hour period using incremental analysis updating (Bloom et al., 1996) and the model is subsequently integrated for a further 6.5 days. The process is then repeated sequentially for the duration of the experiment.

The BRAN version 2p2 experiment described here is a 5-month integration, with the configuration described above. Previous BRAN experiments that are described in the literature include version 1p0 (Oke et al. 2005), version 1p5 (Oke et al., 2008) and version 2p1 (Schiller et al. 2008). A discussion of the differences between each BRAN experiment, and their relative merits, is presented by Oke et al. (2009). At the time of writing, the BRAN2p2 is regarded as the best configuration tested so far. But development and refinement of the Bluelink system is ongoing.

### 3. Results

Between December 2006 and February 2007 there were several wind-driven upwelling events off New South Wales, Australia. The average wind stress during the period of interest is shown in Fig. 2, along with the first empirical orthogonal function (EOF) and its time-series. This figure shows that the average wind

is weakly upwelling favourable during this period. The dominant EOF, accounting for 63% of the total wind stress variance, has virtually no spatial structure but shows that the wind stress variability is generally aligned with the coastline. The wind stress is upwelling favourable when the EOF amplitude (Fig. 2C) is positive. The strong upwelling events can be seen around 23 December, 5 January, and 18 January. A weaker, but longer upwelling event is also evident from 15 February and lasts about a week. There are several other upwelling events that only last for a day or so.

Fig. 3 shows a time series of the 6-hourly wind stress off the central New South Wales coast along with time series of both the reanalysed and observed SLA at several coastal tide gauge stations. The tide gauge observations are low-pass filtered, using a 3-day running mean, and are not assimilated into BRAN2p2, so the good correspondence between the observed and modelled fields provides some independent validation of the realism in the BRAN fields. Fig. 3 shows the response to sea level along the coast, in both the observations and BRAN, with sea-level falling by up to 0.2 m with approximately 1-days lag relative to the strong negative pulses in the meridional wind stress, corresponding to southward upwelling-favourable winds.

Fig. 4 shows comparisons between the 6-day composite observed SST from AVHRR observations processed at CSIRO in Hobart, and daily mean modelled SST fields. The observed AVHRR SST fields are not assimilated by BRAN. Instead, we only assimilate “super-observations” of AMSR-E SST. Super-observations are simply spatially smoothed and sub-sampled observations, as described by Oke et al. (2008). Super-observations are used instead of raw observations to reduce the number of data that are explicitly assimilated, thereby improving the computational throughput of

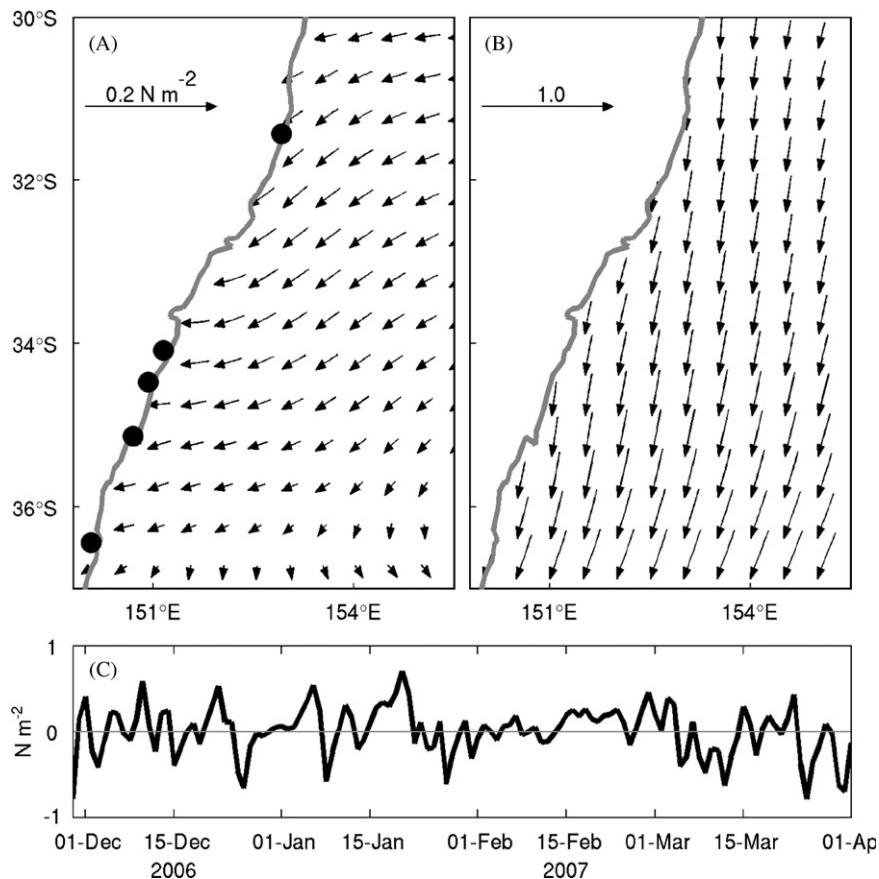
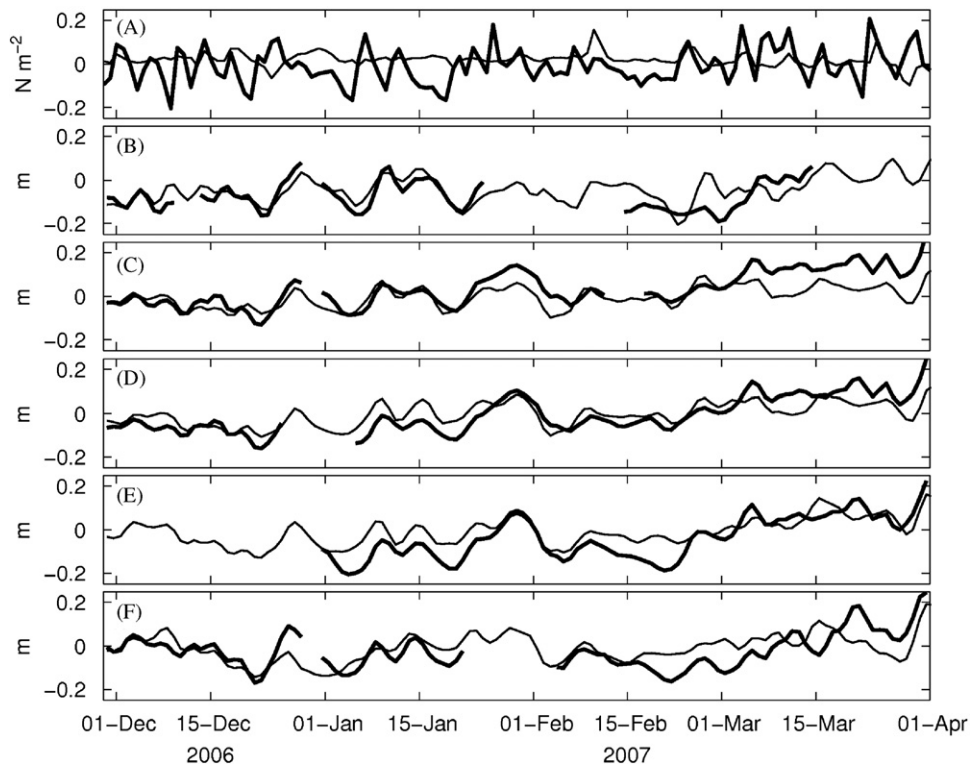


Fig. 2. (A) Time-averaged (11/2007–5/2008) wind stress, (B) dominant EOF of wind stress, and (C) time series of the amplitude of the dominant EOF.



**Fig. 3.** Time series of (A) meridional (bold) and zonal (thin) wind stress at 35.1oS; and (B–F) sea-level anomaly from BRAN (thin) and unassimilated coastal tide gauges (bold). The locations of tide gauges are denoted in Fig. 1.

the assimilation system. We present the AMSRE super-observations, overlaid on the modelled and AVHRR SST fields, in Fig. 4. The circles there denote the location of the AMSRE super-observations and the colour of the circles denotes the value of each super-observation. Note that the AMSRE super-observations do not always match the model or the AVHRR observations. Notably, the AMSRE observations are not available within about 50 km of the coast. Also, the spatial scales resolved by the assimilated AMSRE data are quite coarse. For these reasons, we regard the comparisons between the modelled SST and the high-resolution AVHRR SST fields as an independent assessment of the model's performance. We note that many features evident in the AVHRR observations that are unresolved by the AMSRE super-observations are generally well represented by the model.

Quantitatively, the time-averaged (plus/minus standard deviation) root-mean-squared difference, anomaly correlation, and mean difference between the BRAN SST and the unassimilated AVHRR SST are  $0.2 \pm 0.15$  °C,  $0.6 \pm 0.1$ , and  $0.03 \pm 0.25$  °C, respectively. Some important features can be deduced from Fig. 4 regarding the position and variability of the EAC, the location and orientation of mesoscale features, and the cold coastal upwellings. The position of the EAC is typically denoted by the warm (red) tongue of water that extends adjacent to the coast until about 32°S. South of this point, the EAC usually veers away from the coast – sometimes meandering and reattaching to the coast/shelf (e.g., 20 December, 21 February, Fig. 4) – and sometimes heading south-eastward or even due east (e.g., 24 January, Fig. 4). The mesoscale features in the Tasman Sea are often nicely displayed in SST images. On 17 January (Fig. 4), for example, the cold-core eddy that is the focus of this study can be seen developing at about 153°E and 35°S in both the observations and the model. Fields of SST do not always show mesoscale features, like eddies, very clearly, but sometimes they can be useful for pin-pointing the position of features, or for verifying their existence.

The cold upwellings are most evident between 13 December and 24 January in Fig. 4, corresponding to the upwelling favourable winds that are evident in Fig. 2 and Fig. 3. The model tends to over predict the cold anomalies compared to the observations. This may be a model or wind-forcing error, but it may also be because the model “SST” is the average temperature over the top 10 m, while the satellite sees the temperature at the surface. In general, most features that are evident in the observations are well reproduced in the model. There are periods when the comparisons are not so good, but also periods when the agreement is remarkable.

Profiles of the root-mean-squared difference (RMSD) and mean difference (bias) between Argo profiles of T and S and daily mean fields from BRAN are presented in Fig. 5. Included in these comparisons are the RMSD and bias using climatology. Fig. 5 shows that the BRAN fields are typically closer to observations than climatology. The errors of the BRAN T and S fields at about 300 m, where the variability is very high, are about 1 °C and 0.1 psu respectively, better than climatological estimates, demonstrating that BRAN has some skill at reproducing the true circulation. This is encouraging, given the problematic nature of Eulerian comparisons in regions of strong mesoscale variability, as discussed by Oke et al. (2008).

A series of detailed comparisons between the model and in situ T profiles from Argo in the vicinity of the cold-core eddy of interest here are presented in Fig. 6. These comparisons include profiles of T from climatology, from BRAN, and from Argo. Fortunately, two Argo floats happened to sample the cold-core eddy that is of interest here (see insets of Fig. 6). For individual profiles, the modelled and observed T does not agree perfectly, sometimes with differences of several degrees. Sometimes the model fields are colder than the observations, and sometimes they are warmer. But in each case, both the modelled and observed profiles are much colder than climatology. We suspect that the differences between the model and observations are mostly

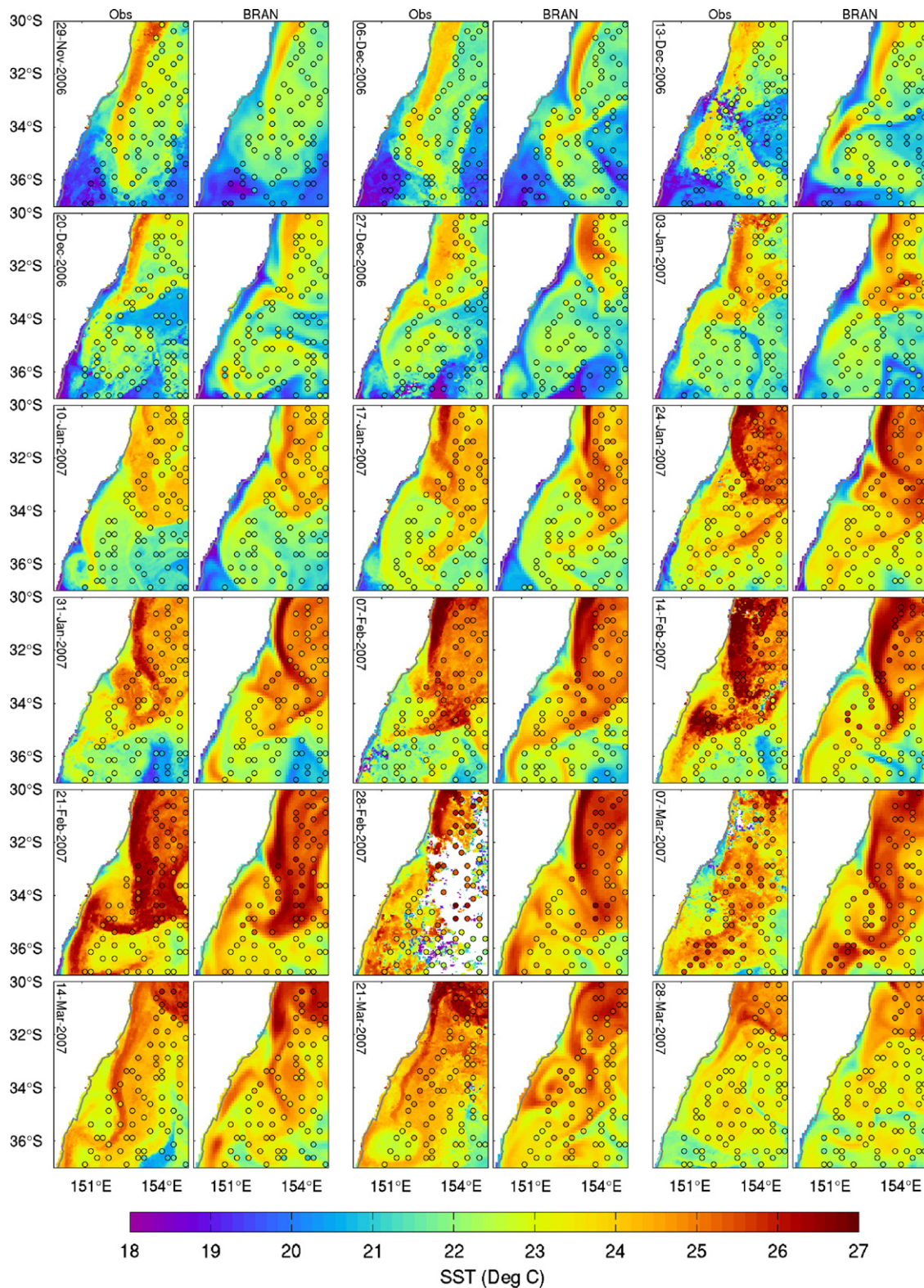


**Fig. 4.** Comparison of observed AVHRR (columns 1, 3 and 5) and reanalysed (columns 2, 4 and 6) SST. The observed AVHRR SST data are not assimilated by BRAN. BRAN assimilates spatially smoothed AMSRE SST observations that are shown by the coloured circles, where the colours denote the AMSRE observation.

related to errors in the position of the eddy in the model. The cold T anomalies evident in Fig. 6 represent upward excursions of isotherms of up to 300 m and these profiles are near the perimeter of the eddy.

A limited number of satellite-tracked surface drifting buoys ([www.aoml.noaa.gov/phod/dac](http://www.aoml.noaa.gov/phod/dac)) were present in the region and

period of interest for this study. This facilitates a qualitative comparison between the drifter-derived circulation and the modelled circulation (Fig. 7). Fig. 7 shows 7-day averages of modelled sea level with 21 days of drifter-derived velocities overlaid. If the model fields are averaged over a longer period, the circulation features are “blurred” because the dominant features

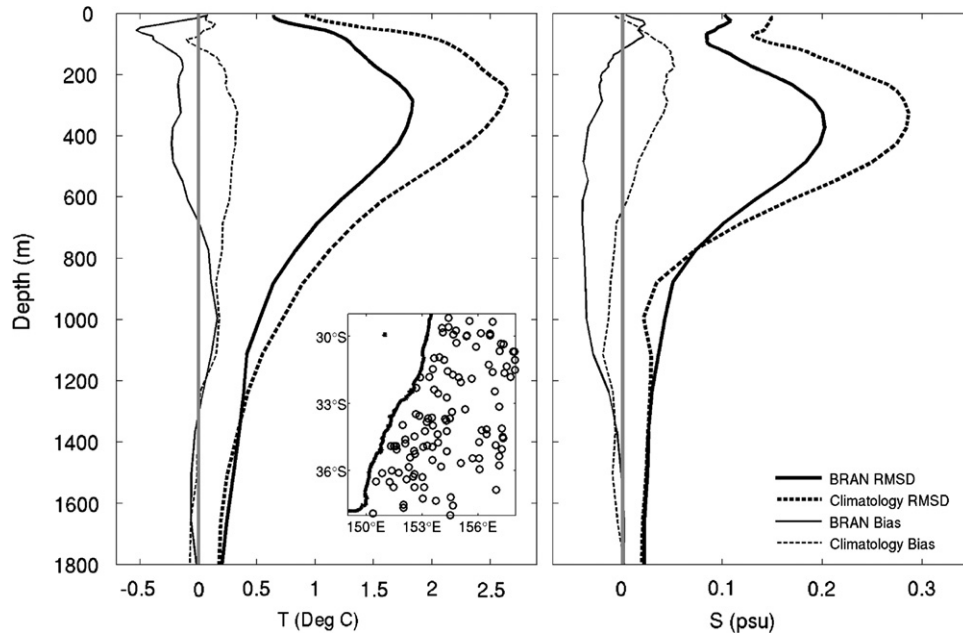


**Fig. 5.** Profiles of the root-mean-squared difference (RMSD; bold lines) and mean difference (Bias; thin lines) between Argo and BRAN (solid lines) and between Argo and climatology (dashed lines) for temperature (left) and salinity (right), based on 120 Argo profiles between 29 November 2006 and 1 May 2007. The distribution of the Argo profiles is shown in the inset of the left panel.

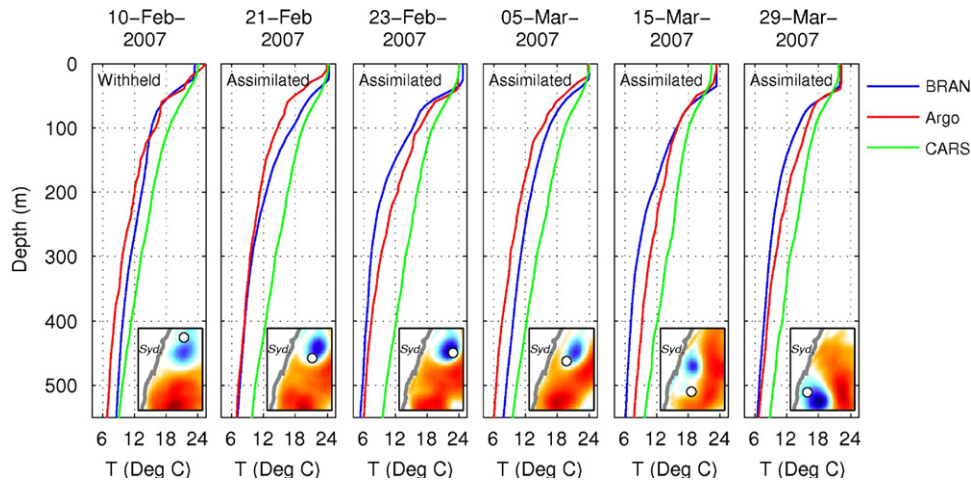


**Fig. 6.** Series of temperature profiles from BRAN (blue), Argo (red) and climatology (green) in the vicinity of the cold-core eddy that developed around 34°S in January 2007. Whether the Argo profile was assimilated or withheld is indicated at the top of each panel. The context of these comparisons and the location of each profile (circle) is given by the daily averaged modelled SLA field in the inset of each panel.

are not completely stationary. Drifter data are included for 21 days to establish a quasi-synoptic picture of the independently observed circulation. Despite the time-misalignment of the earliest and latest drifter data with the model results, the modelled (or, more precisely, the geostrophic component thereof) and observed circulation is generally consistent, with drifters generally following lines of near-constant sea-level. The strongest currents observed from drifters are on the seaward side of the cold-core eddy in February and March 2007.

Finally, an assessment of the model skill is presented in Fig. 8, showing time series of the skill score (e.g., Murphy, 1988; Oke et al., 2002):

$$\text{Skill Score} = 1 - \text{MSE} / \text{MSE}_{ref}, \quad (1)$$

where MSE is the mean-squared error and *ref* denotes a reference field. We regard the best available estimate of the true field to be the analysis that is used for assimilation. We therefore compute the MSE

by differencing the model background field (7 days after assimilation) with the analysis for the same day. We use two different reference fields for comparison here, namely persistence and climatology. Persistence is commonly used in Numerical Weather Prediction, and is where the previous analysis is assumed to persist over time. This is equivalent to using a “model” that does not evolve the circulation over time (i.e. no dynamical model at all). If the skill score relative to persistence is positive, the model has positive skill – that is, it has improved the circulation compared to the previous analysis. If the skill score relative to persistence is zero, the model has no skill; and if the skill score relative to persistence is negative, the model has negative skill – that is, it degrades the circulation compared to the previous analysis. The comparisons with climatology simply evaluate whether the model state is closer to observations than climatological estimates for the same day. Here, we use fields from CARS (Ridgway et al., 2002) for climatology. For a more detailed discussion of skill scores, the reader is referred to Oke et al. (2002).

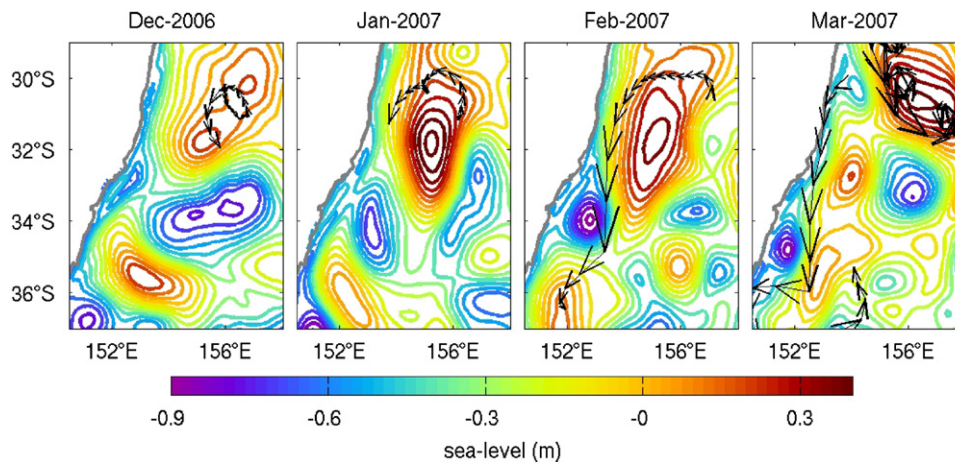


Fig. 7. Contours of modelled sea-level (7-day averages) and observed surface drifter velocities (over 21-days) centred on the 15th of each month.

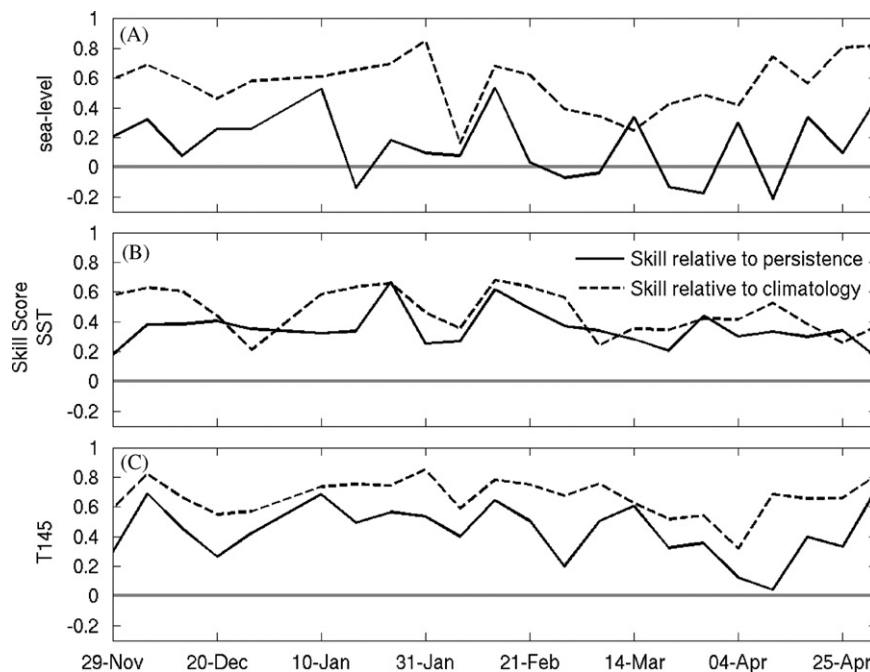


Fig. 8. Time series of the skill score for (A) sea-level, (B) SST, and (C) temperature at 145 m depth, relative to persistence (solid) and climatology (dashed).

We present time series of skill scores for model fields 7-day after each assimilation in Fig. 8 for sea level, SST and temperature at 145 m depth (T145). Skill scores are computed in the domain between 149–156°E and 37–28°S. The results show that for all variables the model tends to have a small amount of skill. For sea level, the skill score relative to climatology is generally quite high, with an average of 0.57, indicating that BRAN often gets the eddies in close-to the right locations. However, the skill score relative to persistence is small, with an average of 0.16, indicating that the model doesn't add very much value to the analyses. The SST skill scores relative to both persistence and climatology are positive throughout the reanalysis, with averages of 0.35 and 0.47 respectively. The skill scores for T145 are also quite high with averages are 0.44 and 0.67 relative to persistence and climatology respectively. Important for this study, the skill for T145 is quite high throughout January and February 2007 (Fig. 8C). This is the time period that we focus on in the dynamical analyses that follow.

Based on the comparisons presented in Fig. 3–Fig. 8, we conclude that the reanalysis captures the circulation realistically enough to

warrant using it to further understand the details of the dominant features. For a comprehensive, quantitative assessment of BRAN, the reader is referred to Oke et al. (2008) where it is shown that the reanalysed fields in the region around Australia are typically within 6–12 cm of withheld altimetric observations, within 0.5–0.9° of observed SST, 4–7 cm of observed coastal sea level, 1° of observed sub-surface temperature, 0.15 psu of observed sub-surface salinity and within 0.2 m s<sup>-1</sup> of near-surface currents. We now turn to an analysis of the reanalysed circulation.

## 4. Analysis

### 4.1. Role of data assimilation

The time-evolution of the cold-core eddy is well represented by a sequence of SLA and temperature anomalies at 145 m depth (T145; Fig. 9). The variability presented in Fig. 9 is reminiscent of the so-called eddy mode, identified by Wilkin and Zhang (2007).

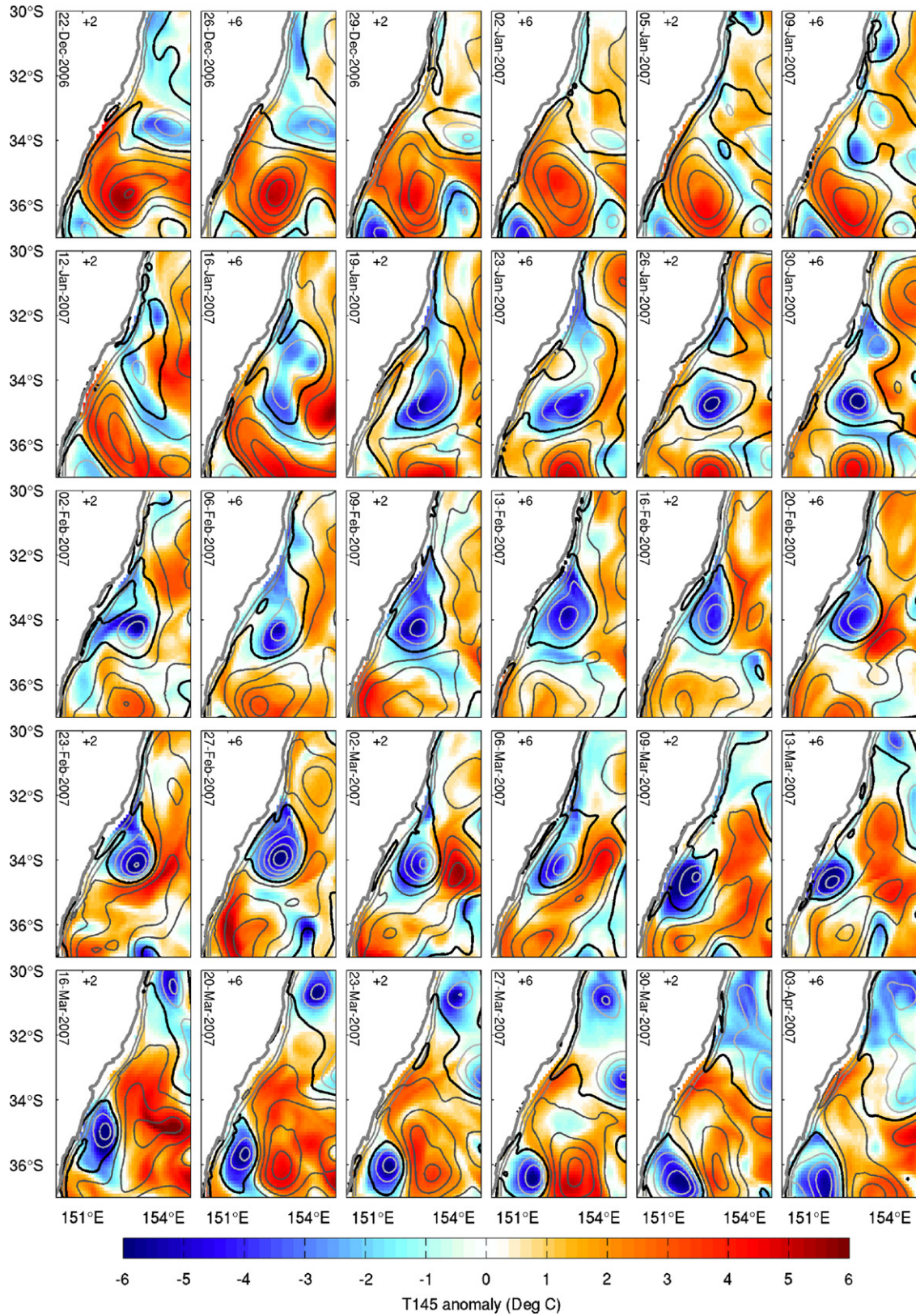


**Fig. 9.** Time sequence of SLA (contoured; intervals=0.2 m) and temperature anomalies at 145 m depth (colour). The dates of each panel are labelled, along with the time relative to the last assimilation update (e.g., +2 indicates that the last assimilation was performed 2 days prior to the current date).

This sequence shows the cold-core eddy develop around 35°S in mid-January. The intensity of the eddy peaks around 27 February when the SLA is almost  $-1$  m.

An important question for us is whether the cold-core eddy develops in BRAN solely because of the assimilation (i.e., the assimilation system simply “puts” the eddy there) or because of

the model dynamics (i.e., due to a simulated dynamical process). Careful inspection of Fig. 9 suggests that the eddy is certainly present and distinct on 26 January. It is probably present and distinct on 19 January; and it is probably forming between 12 and 16 January. We note that a negative SLA is present in the same position (around 153°E, 35°S) throughout December and into early January, but it is not distinct (i.e. pinched off from other circulation features) or continuous in time (it is not present on 5 January, for example). To assess the extent to which the assimilation simply introduces the eddy into the model, we are particularly interested in the nature of the assimilation increments (the introduced changes) on 10, 17, and 24 January.

Examples of temperature and velocity increments, averaged over the top 200 m of the ocean, are presented in Fig. 10. There is evidence of near-geostrophic balance in the temperature and velocity increments in the examples in Fig. 10. This is an

important characteristic of ensemble-based data assimilation systems. It is possible to interpret the role of assimilation by considering the nature of the increments and the characteristics of the background and analysis fields, before and after assimilation respectively. For the example on 10 January the background field has three small cold-core eddies (CC1, CC2 and CC3) at about 34, 31 and 33°S, respectively, and a large warm-core eddy (WC1) at about 36°S. The increment on 10 January draws CC1 and CC3 together and strengthens WC1. Between the analysis on 10 January and the background field on 17 January the model advects CC2 southwards and maintains CC1. On 17 January, the assimilation increment shifts CC2 farther south to make CC1 into a single larger cold-core eddy (CC3) centred at about 35°S. Between the analysis on 17 January and the background field on 24 January the model maintains CC3, weakens it slightly, and generates a new small anti-cyclonic feature (WC2) and a new small cyclonic feature (CC4) to the north of CC3. On 24 January the assimilation increment largely eliminates the recently formed CC4, maintains WC2, and slightly intensifies CC3. WC1 is maintained throughout this sequence as it moves slowly southwards.

The sequence of background, increment, and analysis fields presented in Fig. 10 demonstrate that the role of assimilation is quite important. Sometimes the assimilation acts to introduce new features, coalesce features together, and eliminate them. Sometimes it acts to shift existing features, or modify their intensity. Similarly, the model acts to perform these functions, as demonstrated by the differences between consecutive analysis and background fields. With regard to the intense cold-core eddy that is the focus of this study, the assimilation plays an important role, particularly on 17 January, when it coalesces two cold-core eddies together forming the intense eddy that is the focus of this study. The role of the model is clear between 23–26 February in Fig. 9, when the SLA notably reduces in the centre of the cold core eddy. This is in between assimilation updates and so it is directly attributable to the model dynamics.

The relative contributions of the model and assimilation to the time-evolution of the circulation can be assessed by calculating the “model increment” and the “assimilation increment”. Let us define the percentage change due to the model as:

$$\left| \Delta^{\text{model}} \right| / \left[ \left| \Delta^{\text{model}} \right| + \left| \Delta^{\text{assim}} \right| \right] \times 100,$$

where  $\Delta$  denotes a change,  $||$  denotes an absolute value, and the change due to the model is:

$$\Delta^{\text{model}} = BG^n - AN^{n-1}$$

That is, the change due to the model is the difference between the current background field  $BG^n$  and the previous analysis  $AN^{n-1}$ , and the change due to assimilation is:

$$\Delta^{\text{assim}} = AN^n - BG^n$$

and the superscripts  $n$  and  $n-1$  refer to the assimilation cycle. The sum of the model and assimilation contribution is 100. The average percentage change over an assimilation cycle that can be attributed to the model and the assimilation, computed over the period 29 November 2006 and 2 May 2007, is computed for sea level (left), SST (middle) and T145 (right) in Fig. 11. This analysis shows that the model and assimilation have roughly equal contributions to the reanalysed circulation. For the region of interest, the area-average contribution due to the model for sea-level, SST, and T145 is 50%, 54% and 53%, respectively. Ideally, for a skilful model, the contribution of the model would out-weight that of the assimilation. That is, a good model should require only small adjustments to stay on track. However, for this region, where the circulation is very complex, it is not clear how realistic

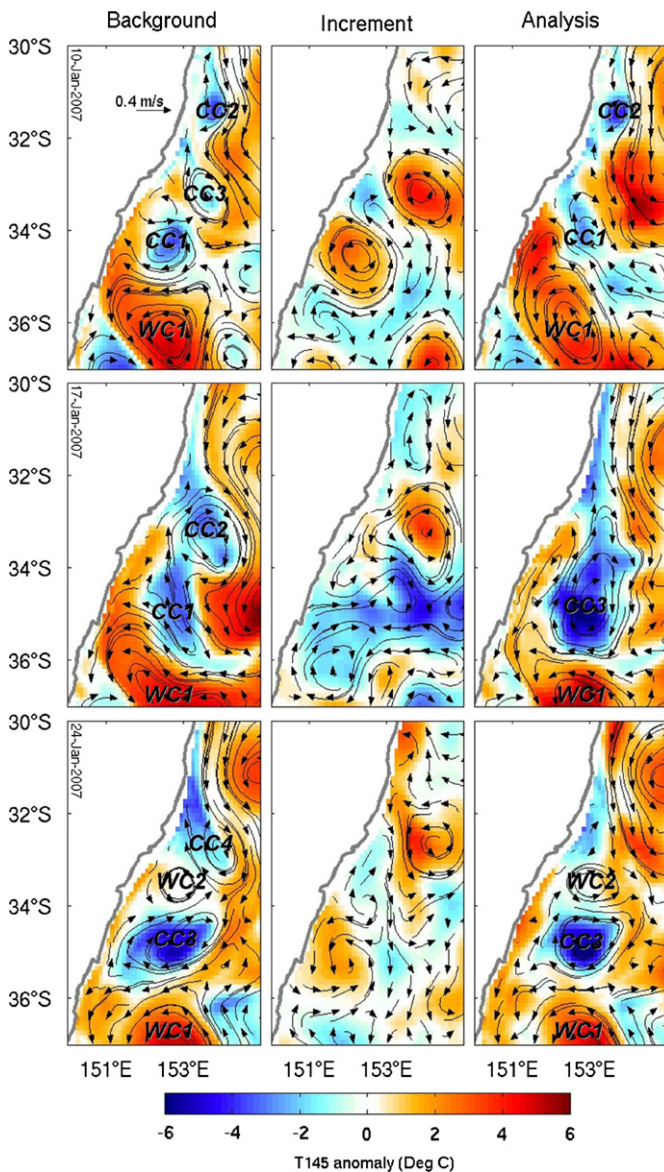


**Fig. 10.** Examples of the background field (left), increments (middle) and analyses (right) for temperature at 145 m depth. The background and analyses are presented as anomalies from a seasonal climatology. The relationship between these fields for a given time is that an analysis equals the background plus the increment. The dates for each example shown are given in the left column. The labels CC1–4 and WC1–2 denote the cold-core and warm-core features referred to in the text.

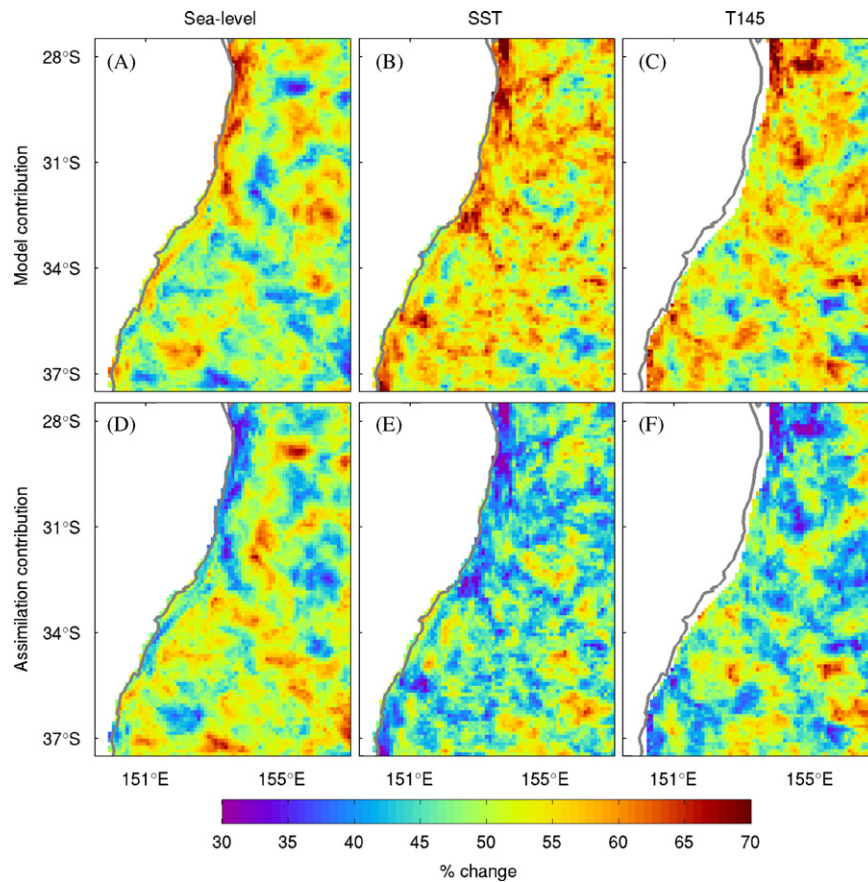


**Fig. 11.** Average percentage change over an assimilation cycle that can be attributed to (A–C) the model and (D–F) the assimilation, computed over the period 29 November 2006 and 2 May 2007, for sea-level (left), SST (middle) and temperature at 145 m depth (T145; right). The percentage change due to the model is  $|\Delta^{\text{model}}| / [|\Delta^{\text{model}}| + |\Delta^{\text{assim}}|] \times 100$ , where  $\Delta$  denotes a change,  $\Delta^{\text{model}} = BGn - AN^{n-1}$  is the change due to the model,  $\Delta^{\text{assim}} = AN^n - BG^n$  is the change due to assimilation,  $BG$  is the background field,  $AN$  is the analysis,  $||$  denotes an absolute value, and the superscripts  $n$  and  $n-1$  refer to the assimilation cycle.

this expectation is. We expect that regions of high eddy variability are always likely to require fairly significant adjustments through assimilation because of the inherently unpredictable nature of the dominant physical processes.

#### 4.2. Eddy structure

Several aspects of the three-dimensional structure of the cold-core eddy, as depicted in BRAN, are shown in Fig. 12. These fields indicate that the currents associated with the eddy often exceed 1.2 m/s, sometimes penetrating all the way to the ocean floor. This indicates that there is a significant barotropic component to the eddy, in addition to the baroclinic component that is manifest in the doming of isopycnals by around 600 m at the centre of the eddy. Fig. 12 also suggests that the eddy is “leaning” to the west-north-west – directly landward. This lean is most clearly seen in the zero velocity contour in the cross-isobath section on 13 February, in Fig. 12.

An analysis of the time variations of the eddy lean is presented in Fig. 13. For simplicity, the lean is here defined as the horizontal distance between the eddy centre at the sea floor and at each depth over the water column. The eddy centre at each depth is estimated from the location of the minimum speed of the currents (note the speed at the centre of a cyclone approaches zero). The time-averaged lean of the eddy is characterised by an offset of about  $28 \pm 15$  km (Fig. 13E–G). That is, the average lean of the eddy at its centre is about 28 km over the 4.5 km deep ocean. This indicates that the eddy is not the vertical, rotating solid body that

we might have imagined. In fact, if we consider the true aspect ratio, the eddy axis is more horizontal than vertical. A  $10^{-6}$  scale model of the 100 km diameter, 4.5 km deep, 30 km vertically offset eddy is the size and shape of a 3 cm misaligned pile of 5 1-mm thick DVDs. If the middle DVDs could be made to bow upwards (about half the thickness of a DVD) this would represent the doming of isopycnals.

Also plotted in Fig. 13 is an estimate of the time-varying distance between the eddy centre at the surface and the coastline and continental shelf, where the position of the 200 m isobath is used to represent the edge of the continental shelf. Fig. 13 indicates that as the eddy moves closer to the continental shelf, it leans to the west (see the zonal lean) and a little bit to the north (see the meridional lean) – that is, it leans directly in towards the coast and into the oncoming EAC as it flows offshore. This lean in the eddy is characteristic of baroclinic instability (e.g., Fujii et al., 2008) that may explain the mechanism for the generation and intensification of the eddy. This characteristic of eddies in the North Pacific Ocean was well observed by Roemmich and Gilson (2001). They constructed composites of cold- and warm-core eddies along high-resolution XBT transects to show that the eddies typically lean to the west by  $0.8^\circ$  longitude over the top 400 m of the water column.

The three-dimensional structure of the eddy is further explored in Fig. 14. Fig. 14 attempts to “unwrap” the eddy, showing fields of potential density, and horizontal and vertical velocity around the perimeter of the eddy. The path around the eddy is chosen by identifying approximately-closed Lagrangian particle paths around the eddy. The horizontal velocity around the

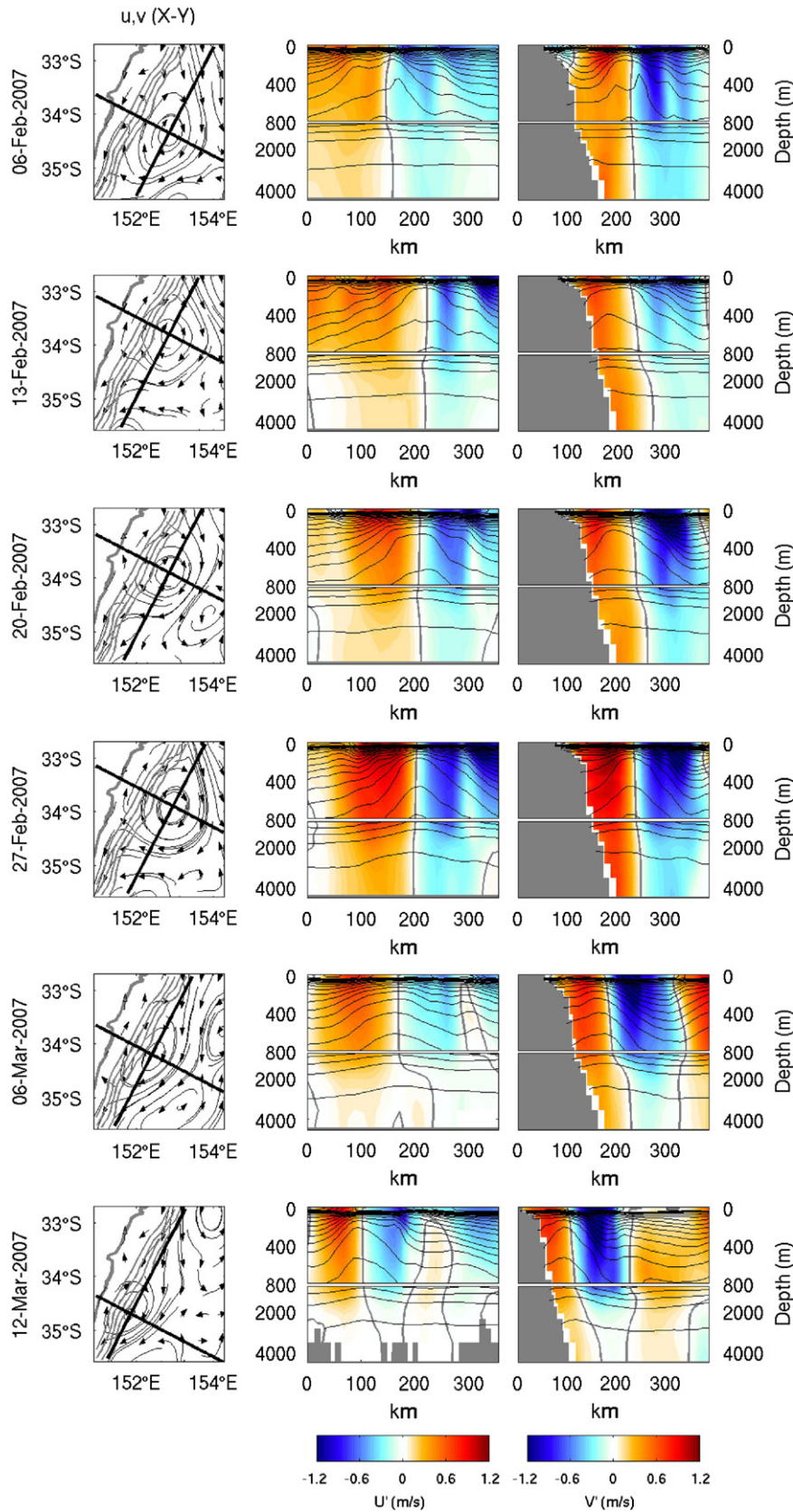


**Fig. 12.** Column 1: Lagrangian trajectories, representing 3-day paths, using the horizontal velocities averaged over the top 200 m; grey contours denote the sea floor topography (contour interval=1000 m). Column 2-3: Potential density (lines; contour interval= $0.2 \text{ kg m}^{-3}$ ) and velocities (colour; grey line denotes zero velocity contour) that are normal to the bold lines marked in column 1. Column 2 shows the more north-south aligned section and column 3 shows the more east-west aligned section. Note the two-stage depth axis.

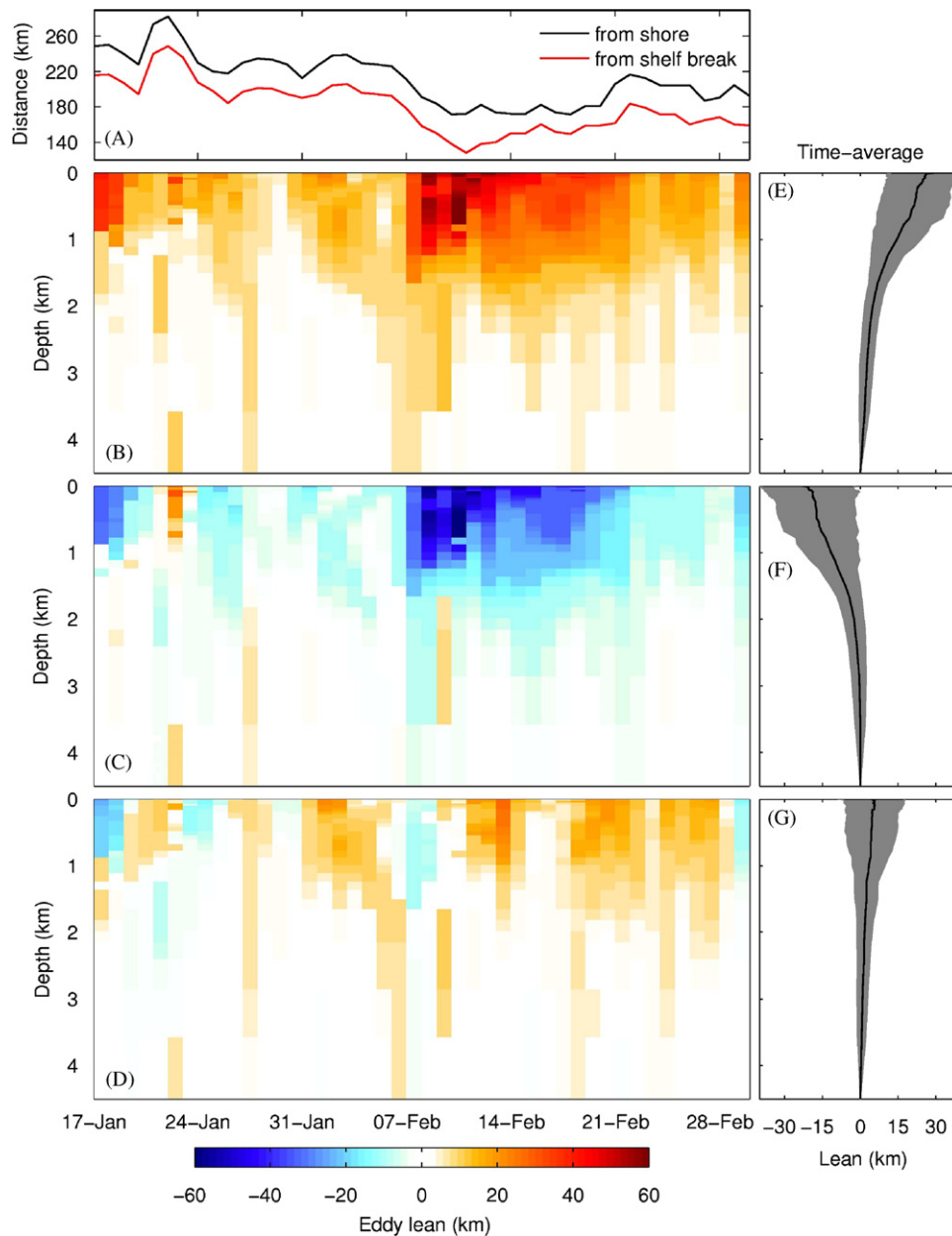


**Fig. 13.** A time sequence of (A) distance of the eddy-centre from shore and from the shelf break; (B) the total lean, (C) the zonal lean and (D) the meridional lean of the eddy over the full depth of the ocean.

eddy penetrates over the full water depth – from the surface to the ocean’s abyss. Where the flow has a positive landward component, the vertical velocity is upward. This vertical velocity (Fig. 14, columns 2 and 3) extends over most of the water column. At some depths, water parcels travelling around the eddy undergo 100 m vertical excursions – coming closest to the surface where the topography is shallowest. The rotational axis of the eddy is therefore tilted away from the land. This angle, however, is much less ( $\sim 100$  m/100 km) than the landward tilt (28/4.5 km) of the axis defined by the points of zero velocity. So, referring back to the DVD analogy introduced above – the 3-cm-offset stack of 5 DVDs is not perfectly horizontal.

To better understand the likely cause of the vertical circulation around the eddy we present maps of sea level along with the vertical and horizontal velocity vertically averaged between 0–500, 500–1000, 1000–2000, and 2000–4500 m, and averaged over time between 19 January and 6 February 2009 (Fig. 15) and

between 9 February and 27 February (Fig. 16). Note that the water velocities associated with the eddy penetrate over the full depth of the ocean – to 4500 m depth. Note also that on the shoreward side of the eddy, the current speed has a local maximum between 2000–4500 m. This local maximum is stronger in mid- to late-February (Fig. 16) than it is in late January and early February (Fig. 15). We note that the eddy is closer to the continental shelf and slope in Fig. 16 than it is in Fig. 15. We suspect that as the eddy moves towards the coast, the deep currents associated with the barotropic pressure gradient are forced to accelerate as they approach the deep continental slope. At the same time, some water flows up the slope. This is evident in the strong vertical velocities in the deep ocean adjacent to the deep continental slope (Fig. 16D). This upward motion penetrates over the entire water column, resulting in large vertical velocities over the mid- and upper-ocean (Fig. 16A–C) and 100 m vertical excursions of isopycnals around the eddy (Fig. 14).

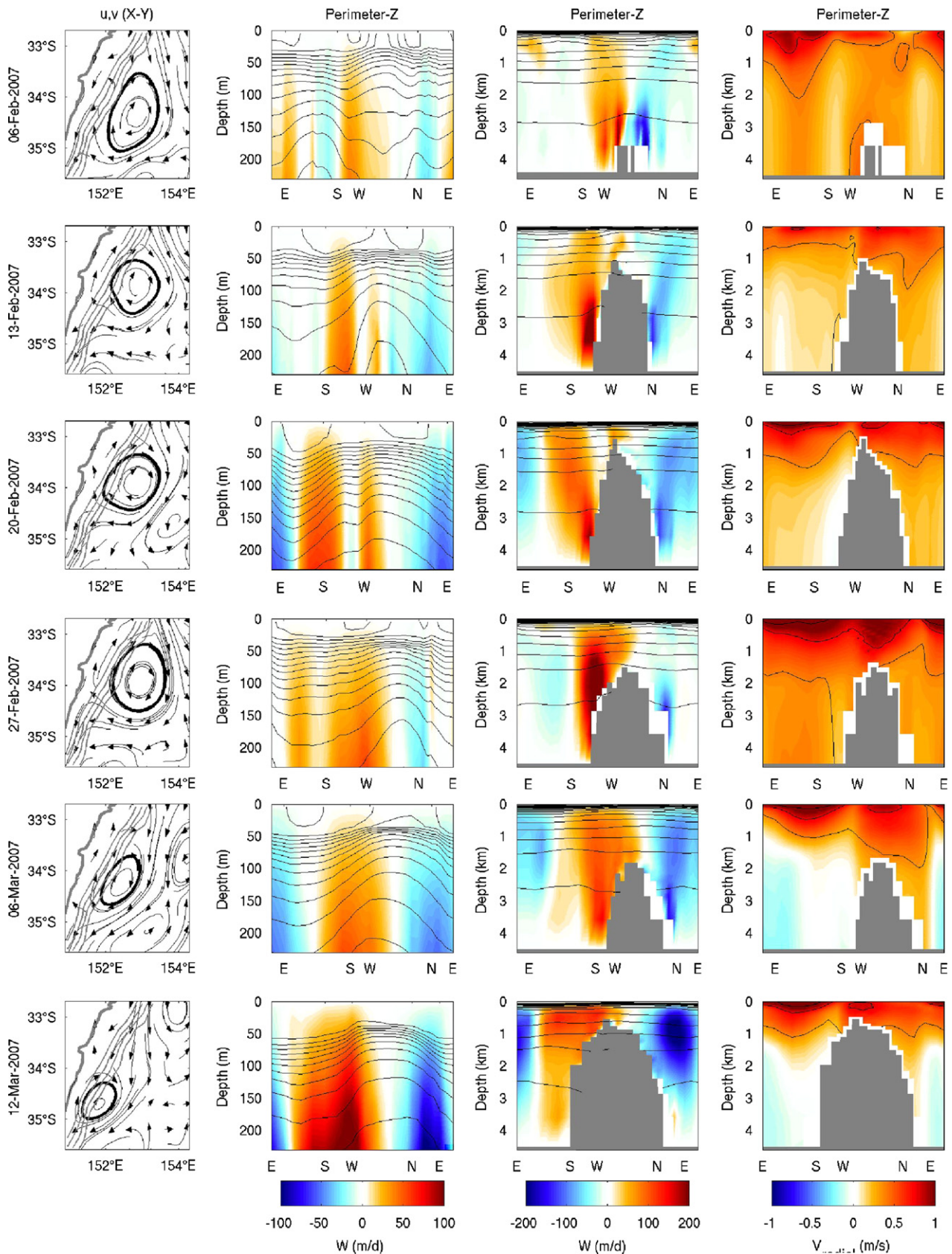


**Fig. 14.** Column 1: Lagrangian trajectories, representing 3-day paths, using the horizontal velocities averaged over the top 200 m; grey contours denote the topography (contour interval=1000 m). Column 2: Vertical velocity (colour; red is upwelling, blue is downwelling) with isopycnals overlain (lines; contour interval= $0.2 \text{ kg m}^{-3}$ ) for a section around the perimeter of the cold-core eddy over the top 250 m of the ocean. The location of the perimeter is denoted in bold in column 1. Column 3: As for column 2, except for the full water depth. Column 4: Radial velocity, around the eddy perimeter (positive is clockwise; grey line denotes the zero contour). Each row corresponds to a different date that is marked to the left of each row.

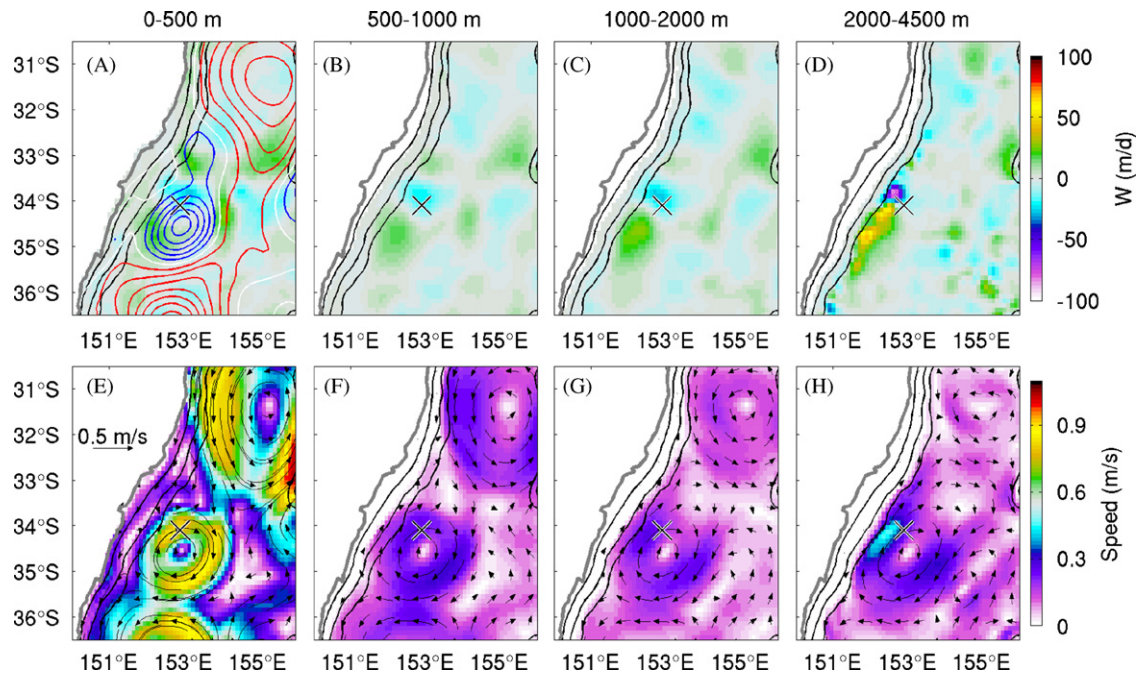


**Fig. 15.** (A–D) Vertical velocity and (E–H) horizontal velocities, vertically averaged between (A,E) 0–500 m; (B,F) 500–1000 m; (C,G) 1000–2000 m; and (D,H) 2000–4500 m; and time-averaged between 19 January and 6 February 2009. The velocity vectors are shown in panels (E–H) and the colour is speed. SLA is contoured in panel (A) (blue is negative, red is positive, white is zero, contour interval is 0.2 m). The 200, 1000 and 4000 m isobath is contoured in each panel.

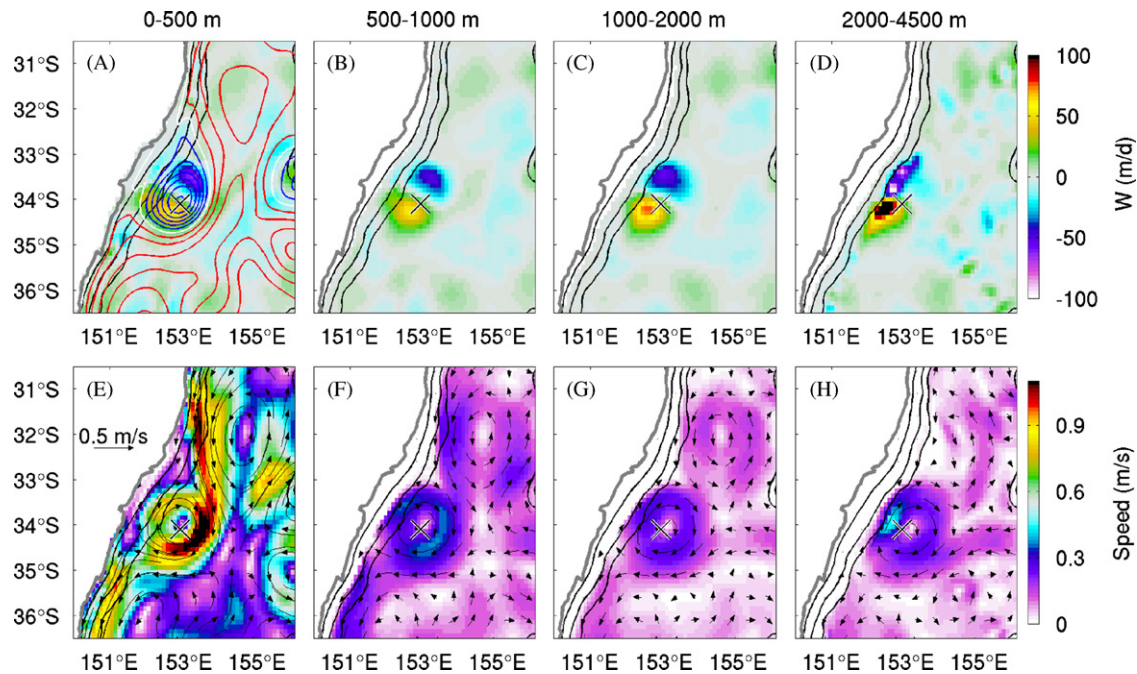


**Fig. 16.** As for Fig. 15, except for fields averaged between 9 February and 27 February 2009.

#### 4.3. Eddy generation and intensification

The time sequence of SLA and T145 anomaly maps in Fig. 9 show cold anomalies being generated adjacent to the continental shelf during upwelling favourable winds. The cold anomalies become entrained in the EAC, are advected southwards and appear to coalesce with the cold-core eddy. The first such event begins on 5 January, during upwelling favourable winds (Fig. 3A). The cold anomaly is first evident at 30°S on 5 January. It becomes entrained into the EAC and is advected southwards. Over the

following 2 weeks, the cold anomaly is advected southwards and then moves offshore at the same time as the cold-core eddy develops on 19 January at about 34°S and 153°E (Fig. 9). A similar sequence of events occurs immediately after this. Another cold anomaly appears adjacent to the continental shelf on 19 January at about 32°S during another period of upwelling favourable winds (Fig. 3A). Again, the cold anomaly is entrained into the EAC, is advected southwards and offshore, before coalescing with the cold-core eddy (Fig. 9). These sequences are particularly clear in an animation of SLA and T145 anomaly fields. A similar event

appears to start on 13 March, although in this case the cold water mass doesn't make it to the cold-core eddy because the eddy has moved off to the south by then.

The southward advection of cold upwelled water along the path of the EAC, and its subsequent coalescence into the cold-core eddy leads us to speculate about a possible link between the upwelling and the eddy formation. Is the eddy simply a reservoir for cold upwelled water that originates to the north in response to wind-driven upwelling? Does the advection of cold water trigger an instability that results in the eddy? By calculating a time series of the eddy kinetic energy (EKE) and the available potential energy associated with the upwellings and the eddy (not shown), we can quickly rule out this hypothesis. The available potential energy over the continental shelf and slope associated with the upwellings is an order of magnitude smaller than the available potential energy and EKE associated with the eddy – as are the tendencies of these fields. The eddy is therefore not merely an accumulation of cold upwelled water.

The role of the upwellings, and specifically the introduction of the upwelled water into the vicinity of the developing, or developed, eddy are less clear. Consideration of the role of assimilation (Fig. 10 and Fig. 11) indicates that assimilation plays a key role in organising the cold-core eddy. However, the model also plays an important role in maintaining the eddy and subsequently intensifying it. An example of this intensification can be seen in Fig. 9, between 23–27 February, when the eddy intensifies due to model dynamics, not due to assimilation. Several aspects of the circulation support the likelihood of an instability. For example, the circulation is characterised by relatively high Rossby number, during the period of eddy generation. The vorticity ( $\zeta = dv/dx - du/dy$ , where  $[u, v]$  are the zonal and meridional velocities in the  $[x, y]$  directions) scales like  $U/L$ , where  $U$  is a scale for horizontal velocity and  $L$  is a horizontal

length scale. The magnitude of the vorticity divided by the absolute value of the Coriolis parameter  $\xi/|f|$ , provides an estimate of the local Rossby number  $Ro = U/(|fL|)$ . When  $Ro$  is large (near 1) the non-linear advection terms in the momentum equations are important. That is, the circulation is likely to be ageostrophic. The daily-average  $\xi/|f|$  fields, averaged over the top 200 m, are shown in Fig. 17 during the period of eddy generation. This figure shows that for much of the period of interest, the magnitude of  $\xi/|f|$  is relatively small, with magnitudes of less than 0.5. However, the magnitude of  $\xi/|f|$  is large after the cold-core eddy is established off Sydney (22 January 2007) and again during the intensification of the eddy (26 February). This indicates that the circulation is non-linear, possibly with significant interactions between the eddy and the EAC.

The fields in Fig. 17 indicate that the circulation is non-linear around the time that the eddy is formed and during the subsequent intensification. There are strong horizontal gradients of the mean flow, separating the EAC from adjacent Tasman Sea water masses evident in the complicated vorticity fields. These strong horizontal gradients may result in barotropic instability, where mean kinetic energy is converted to EKE, as suggested by Bowen et al. (2005). The EAC circulation is also vertically sheared, and may therefore experience baroclinic instability, where available potential energy is converted to EKE. The lean of the eddy, noted in Fig. 12, is a typical characteristic of baroclinic instability (e.g., Jochum et al., 2004; Fujii et al., 2008).

## 5. Discussion

Although eddies have been observed to lean over (Roemmich and Gilson, 2001), the eddy that is studied here leans over more than we expected. Indeed, conceptual models of eddies often depict them as solid-bodies that rotate as a vertical column (e.g., Lee et al., 1991; McGillicuddy et al., 1998; Campos et al., 2000). This is clearly not the case here, with the position of the eddy centre at the surface, and at depth sometimes being separated by as much as 60 km (about half the eddy diameter) over an ocean that is 4.5 km deep. If we consider the true aspect ratio, the eddy axis (defined by the points of zero horizontal flow) is more horizontal than vertical.

The vertical circulation around the eddy is not consistent with the standard conceptual models of upwelling at the centre of a cold-core eddy (e.g., Lee et al., 1991; McGillicuddy et al., 1998). The maximum vertical displacement of isopycnals, which is upwards by 600 m at some depths, occurs at the centre of the eddy, but the maximum vertical velocities occur at mid-radius, associated with water parcels ascending about 100 m where the flow is climbing the continental slope, and descending again where it flows back off the continental slope.

It is not clear whether the vertical velocity in the reanalysis is realistic – we have no direct way of assessing it. However, we note that qualitatively similar vertical velocity fields have been inferred from observations of the Gulf Stream (Osgood et al., 1987; Lee et al., 1991) and the Brazil Current (Campos et al., 2000; see their Fig. 1). In both cases, estimates of vertical velocity fields associated with poleward propagating cold-core eddies have noted upwelling at the leading edge of the eddy, and downwelling at the trailing edge. These studies cite the propagation of eddies as a key characteristic. We note that for the case studied here, the cold-core eddy is almost stationary during much of the analysis period. However, when the eddy does start to move polewards in March 2007 (Fig. 14, Fig. 15, and Fig. 16), the vertical velocities are stronger, so the mechanism described by Lee et al. (1991) and Campos et al. (2000) probably plays a key role in the dynamics modelled here.

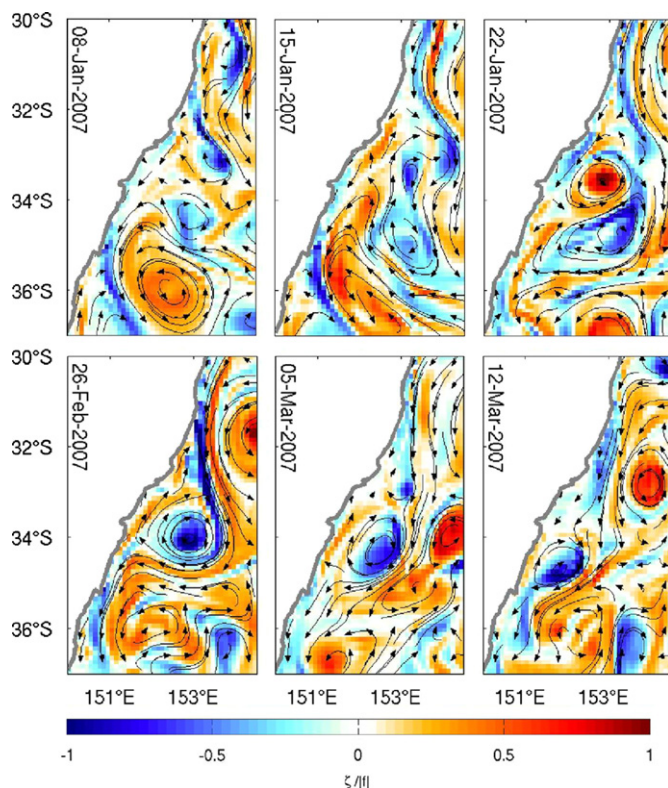


Fig. 17. Estimates of the Rossby number, approximated by the surface vorticity divided by the absolute value of the Coriolis parameter, during the period of eddy generation (top row) and the subsequent intensification (bottom row).

Campos et al. (2000) draw on the upwelling/downwelling circulation around propagating cold-core eddies in the Brazil Current to explain nutrient enrichment of shelf waters. They argue that because the water being downwelled and moved offshore on the trailing edge of the eddy is not necessarily the same water that is upwelled and driven onshore by the leading edge, there is a new deposition of upwelled water on the shelf. This could also be true for the case examined here. Evidence for this is found in satellite images of ocean colour (Fig. 18), showing ribbons of relatively high Chl-a around the eddy's perimeter. The vectors displayed in Fig. 18 represent Lagrangian paths over three days, based on the surface velocities from the model. These velocity fields indicate that at mid-radius, a full loop around the eddy takes about 10 days. Blooms take several days to develop, so they will not occur when and where the upwelling is happening, but well away from it. So, we speculate that nutrient-rich waters may be uplifted towards the surface around the eddy, and mixed into the surface layer. Subsequently, as the high-nutrient waters travel around the eddy within the euphotic zone, the phytoplankton may bloom, as evident in the Chl-a fields (Fig. 18). However, we note that there are a number of alternative explanations that may explain the high Chl-a around

the eddy. For example, it could simply be entrainment of upwelled water by the eddy, where the upwelled water is residing on the continental shelf following the strong upwellings that preceded the eddies development.

A rich mesoscale eddy field is a defining characteristic of the EAC region. Many previous scientific studies have been devoted to better understanding the characteristics and evolution of Tasman Sea mesoscale eddies. While most of these have focussed on warm-core eddies (Andrews and Scully-Power, 1976; Nilsson and Cresswell, 1980; Brandt, 1981; Cresswell, 1982, 1983; Tranter et al., 1986; Huyer et al., 1988; Mata et al., 2000; Marchesiello and Middleton, 2000; Mata et al., 2006), some studies have also noted the importance of cold-core eddies (Cresswell, 1974, 1994; Huyer et al., 1988; Gibbs et al., 1997). The significance of cold-core eddies in other western boundary current regions has been noted by many studies (e.g., Lee et al., 1991; Campos et al., 2000). Based on a survey of cold-core eddies reproduced in a 15-year reanalysis (1993–2007), using BRAN2p1 (Schiller et al., 2008), we estimate a frequency histogram of the intensity of all cold-core eddies in the EAC region over the last 15-years (Fig. 19). Specifically, we compute the minimum SLA in the region 150–156°W and 37–30°S, and the maximum negative temperature anomaly directly below each SLA minimum for each day of BRAN2p1. The cold-core eddy that is of interest in this study is characterised by a maximum SLA anomaly of  $-0.9$  m, with a corresponding temperature anomaly of  $-9$  °C. These points are noted in Fig. 19, indicating that the eddy studied here is indeed a very extreme case. Indeed, Thompson et al. (2009) report Chl-a concentrations off Port Hacking during this event as one of the three most extreme events observed during the SEAWIFS satellite era.

Another surprising aspect of the reanalysed circulation is the depth over which the eddy penetrates. We show it penetrating to the ocean floor (Figs. 15 and 16). Direct observations of the abyssal ocean currents in the Tasman Sea are rare. Notable exceptions include the observations reported by Lilley et al. (1986) and Mulhearn et al. (1988). They measured near-bottom velocities of over 0.3 m/s, and found that surface velocities associated with a developing warm-core eddy were well correlated with abyssal velocities. These results indicate that mesoscale circulation in the Tasman Sea may include a significant barotropic component. This is consistent with the results from the reanalysis presented here (Figs. 15 and 16).

We have made some effort in this study to understand the relative roles of assimilation and model dynamics in reproducing the extreme features of interest here. We find that both play important roles. The assimilation appears to dominate the tendency during the initial formation, but the model subsequently intensifies and evolves the eddy. We note that with sequential

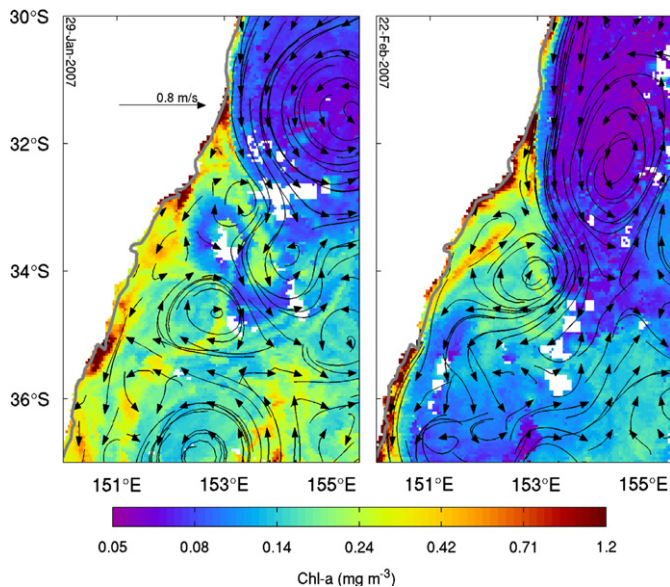


**Fig. 18.** Composite images of Chl-a from MODIS and SeaWiFS data. The corresponding Lagrangian trajectories, representing 3-day paths, using the horizontal surface velocities from BRAN are overlain for reference.

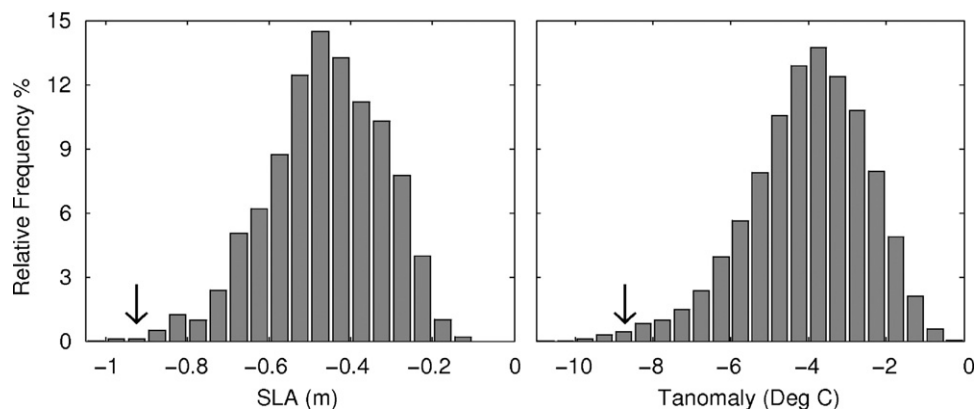


**Fig. 19.** Relative frequency histogram of all cold-core eddies in the Tasman Sea between 1993–2007, computed from the statistics of the minimum SLA for each day of BRAN2p1 (left), and the maximum negative temperature anomaly below each minimum. The characteristics of the eddy studied in this paper are denoted by the arrows.

data assimilation systems, interpretation of dynamical processes is necessarily more complicated than a free model run without assimilation. However, the non-linearity of the flow fields of interest means that assimilation is a “necessary evil” that is required to keep the model in close alignment with reality.

The precise mechanism by which the cold-core eddy of interest here formed and intensified remains somewhat unclear. Investigations of eddies in western boundary current regions attribute eddy formation to processes such as baroclinic instability (e.g., Boudra et al., 1988; Oey, 1988; Lee et al., 1991), barotropic instability (e.g., Jochum and Malanotte-Rizzoli, 2003; Bowen et al., 2005), and mixed barotropic-baroclinic instability (e.g., Hurlburt et al., 1996; Mata et al., 2006). Other mechanisms that have been related to eddy generation include topographic features that perturb boundary current flows, causing meanders and eddies to form (e.g., Singer et al., 1983; Lee et al., 1991), and a so-called flow detachment process (Penven et al., 2001). For the cold-core eddy of interest in this study, we find the conditions surrounding the eddy render the likely generation mechanism to be a baroclinic instability, barotropic instability, or a mixed barotropic-baroclinic instability. This is consistent with the conclusions of Mata et al. (2006), based on analyses of eddy energetics from observations, and Wilkin and Zhang (2007), based on analyses of a regional model of the Tasman Sea.

## 6. Conclusion

With the aid of an eddy-resolving ocean reanalysis, the three-dimensional structure of an extreme cold-core eddy is explored. First, we compare reanalysed fields with assimilated and withheld observations and verify that the model faithfully reproduces the salient observed features of the true circulation. Some of the details of the modelled circulation are clearly different to reality, but in general the reanalysis does a good job of reproducing the main features of interest. These features include the ocean's response to a series of wind-driven upwelling events. This includes decreases of SST of up to 5 °C and sea-level decreases of up to 0.2 m. Following these upwellings, a cold-core eddy develops and intensifies to become one of the most intense cold-core eddies ever observed in the Tasman Sea since the advent of satellite altimeter observations of sea level.

The three-dimensional structure of the cold-core eddy is not what we expected. The currents associated with the eddy penetrate over the entire water column. While this is consistent with some historical observations of mesoscale features in the Tasman Sea (e.g., Lilley et al., 1986; Mulhearn et al., 1988), it is more common to assume that signals associated with eddies diminish more quickly over depth. The reanalysed eddy also shows a distinct lean with the eddy centre at the surface displaced by up to 60 km from the eddy centre at the ocean floor. This is inconsistent with the common conceptual model of eddies being solid, rotating, vertical bodies. Finally, the reanalysed eddy shows large vertical excursions of water parcels that we did not expect. Water parcels at mid-depth ascend by 100 m as they move shoreward over the continental slope, then descend again as they move offshore on their way around the centre of the eddy. We attempt to present a three-dimensional picture of the eddy by “unwrapping” it around its perimeter and to show the vertical velocity and associated vertical excursion of isopycnals. We speculate that this may have taken nutrient-rich water into the euphotic zone, increasing primary production (or making it more visible to the satellite) around the eddy's perimeter. We present maps of normalised Chl-a that seem to support this possibility.

The strong horizontal shears in the EAC flow when the eddy forms suggest that the eddy may be generated through a process

of barotropic instability. However, the vertical shears associated with the EAC render baroclinic instability a likely mechanism – and the characteristic lean of the eddy is also consistent with baroclinic instability. Regardless of the precise dynamics by which the eddy forms, the timing of this instability, immediately after the “arrival” of a cold upwelled water mass into the vicinity, leads us to suspect that this disturbance played a role in triggering the instability – though we cannot be sure of this relationship.

The events of Austral summer 2006–07 were extreme in many respects. The magnitude and frequency of wind-driven upwellings were unusual. The intensity of the ensuing cold-core eddy was almost a record. We have used a data assimilating model to provide a complete three-dimensional time-varying picture of the ocean circulation during these events. We present a quantitative assessment of the reanalysed circulation, showing that reanalysed SST is typically within 0.2 °C of withheld SST observations and that the model has positive skill compared to both climatology and persistence for key variables. However, not all aspects of the reanalysis system can be verified. For example, we have analysed the vertical circulation in the model and tried to relate it to other independent observations. We believe that the data assimilating model is a useful tool for synthesising observations, and extrapolating them to unobserved regions and variables. As a result of this effort, our conceptual picture of cold-core eddies in the Tasman Sea has changed. They are much more complex than we expected.

## Acknowledgments

Financial support for this research is provided by CSIRO, the Bureau of Meteorology, and the Royal Australian Navy as part of the Bluelink project, the US Office of Naval Research (Grant No. N00014-07-1-0422), and the Australian Research Council (Discover Grant DP0988818). The authors also gratefully acknowledge useful discussions with M. Baird and the many contributions of the Bluelink science team. Satellite altimetry is provided by NASA, NOAA, ESA and CNES. Drifter data are provided by NOAA-AOML and SST observations are provided by NASA, NOAA and Remote Sensing Systems.

## References

- Ajani, P., Hallegraef, G.M., Pritchard, T., 2001. Historic overview of algal blooms in marine and estuarine waters of New South Wales, Australia. *Proceedings of the Linnean Society of New South Wales* 123, 1–22.
- Andrews, J.C., Scully-Power, P., 1976. The structure of an East Australian current anticyclonic eddy. *Journal of Physical Oceanography* 6, 756–765.
- Baird, M.E., Timko, P.G., Wu, L., 2007. The effect of packaging of chlorophyll within phytoplankton and light scattering in a coupled physical–biological ocean model. *Marine and Freshwater Research* 58, 966–981.
- Blackburn, S.I., Cresswell, G.R., 1993. A coccolithophorid bloom in Jervis Bay, Australia. *Australian Journal of Marine and Freshwater Research* 44, 253–260.
- Bloom, S.C., Takas, L.L., Da Silva, A.M., Ledvina, D., 1996. Data assimilation using incremental analysis updates. *Monthly Weather Review* 124, 1256–1271.
- Boudra, D., Bleck, R., Schott, F., 1988. A numerical model of instabilities in the Florida current. *Journal of Marine Research* 46 (4), 715–751.
- Bowen, M.M., Wilkin, J.L., Emery, W.J., 2005. Variability and forcing of the East Australian current. *Journal of Geophysical Research* 110, C03019. doi:10.1029/2004JC002533.
- Brandt, S.B., 1981. Effects of a warm-core eddy on fish distributions in the Tasman Sea off East Australia. *Marine Ecology* 6, 19–33.
- Brassington, G.B., Pugh, T., Spillman, C., Schulz, E., Beggs, H., Schiller, A., Oke, P.R., 2007. BLUElink development of operational oceanography and servicing in Australia. *Journal of Research and Practice in Information Technology* 39, 151–164.
- Campos, E.J.D., Velhote, D., da Silveria, I.C.A., 2000. Shelf break upwelling driven by Brazil current cyclonic meanders. *Geophysical Research Letters* 27, 751–754.
- Chen, D., Rothstein, L.M., Busalacchi, A.J., 1994. A hybrid vertical mixing scheme and its application to tropical ocean models. *Journal of Physical Oceanography* 24, 2156–2179.

- Cresswell, G.R., 1974. Ocean currents measured concurrently on and off the Sydney area continental shelf. *Australian Journal of Marine and Freshwater Research* 25, 427–438.
- Cresswell, G.R., 1982. The coalescence of two East Australian Current warm-core eddies. *Science* 8, 161–164.
- Cresswell, G.R., 1983. Physical evolution of Tasman Sea Eddy J. *Australian Journal of Marine and Freshwater Research* 34, 495–513.
- Cresswell, G.R., 1994. Nutrient enrichment of the Sydney continental shelf. *Australian Journal of Marine and Freshwater Research* 45, 677–691.
- Fujii, Y., Tsujino, H., Usui, N., Nakano, H., Kamachi, M., 2008. Application of singular vector analysis to the Kuroshio large meander. *Journal of Geophysical Research*, 113. doi:10.1029/2007JC004476.
- Gibbs, M.T., Marchesiello, P., Middleton, J.H., 1997. Nutrient enrichment of Jervis Bay, Australia, during the massive 1992 coccolithophorid bloom. *Marine and Freshwater Research* 48, 473–478.
- Griffies, S.M., Hallberg, R.W., 2000. Biharmonic friction with a Smagorinsky-like viscosity for use in large-scale eddy-permitting ocean models. *Monthly Weather Review* 128, 2935–2946.
- Griffies, S.M., Pacanowski, R.C., Rosati, A., 2004. A technical guide to MOM4. GFDL Ocean group technical report No 5. 5. NOAA/Geophysical Fluid Dynamics Laboratory 371pp.
- Hallegraef, G.M., Jeffrey, S.W., 1993. Annually recurrent diatom blooms in spring along the New South Wales Coast of Australia. *Australian Marine and Freshwater Research* 44, 325–334.
- Hurlburt, H.E., Wallcraft, A.J., Schmitz Jr., W.J., Hogan, P.J., Metzger, E.J., 1996. Dynamics of the Kuroshio/Oyashio current system using eddy-resolving models of the North Pacific Ocean. *Journal of Geophysical Research* 101 (C1), 941–976.
- Huyer, A., Smith, R.L., Stabeno, P.J., Church, J.A., White, N.J., 1988. Currents off South-eastern Australia: Results from the Australian Coastal experiment. *Australian Journal of Marine and Freshwater Research* 39, 245–288.
- Jochum, M., Malanotte-Rizzoli, P., 2003. On the generation of North Brazil current rings. *Journal of Marine research* 61, 147–173.
- Jochum, M., Malanotte-Rizzoli, P., Busalacchi, A., 2004. Tropical instability waves in the Atlantic Ocean. *Ocean Modelling* 7, 145–163.
- Kallberg, P., Simmons, A., Uppala, S., Fuentes, M., 2004. The ERA-40 archive, European centre for medium-range weather forecasts (ECMWF), ECMWF Re-Analysis Project (ERA), ERA-40 Project Report Series 17, 31pp.
- Lee, T.N., Yoder, J.A., Atkinson, L.P., 1991. Gulf Stream frontal eddy influence on productivity of the southeast U.S. continental shelf. *Journal of Geophysical Research* 96, 22191–22205.
- Lilley, F.E.M., Filloux, J.H., Bindoff, N.L., Ferguson, I.J., Mulhearn, P.J., 1986. Barotropic flow of a warm-core ring from sea-floor electric measurements. *Journal of Geophysical Research* 91, 12979–12984.
- Macdonald, H.S., Baird, M.E., Middleton, J.H., 2009. Effect of wind on continental shelf carbon fluxes off southeast Australia: A numerical model. *Journal of Geophysical Research* 114, C05016. doi:10.1029/2008JC004946.
- Marchesiello, P., Middleton, J.H., 2000. Modeling the East Australian Current in the western Tasman Sea. *Journal of Physical Oceanography* 30, 2956–2971.
- Mata, M.M., Tomczak, M., Wijffels, S., Church, J.A., 2000. East Australian current volume transports at 30°S: Estimates from the world ocean circulation experiment hydrographic sections PR11/P6 and the PCM3 current meter array. *Journal of Geophysical Research* 105, 28,509–28,526.
- Mata, M.M., Wijffels, S.E., Church, J.A., Tomczak, M., 2006. Eddy shedding and energy conversions in the East Australian current. *Journal of Geophysical Research* 111, C09034. doi:10.1029/2006JC003592.
- McGillicuddy, D.J., Robinson, A.R., Siegel, A.A., Jannasch, H.W., Johnson, R., Dickey, T.D., McNeil, J., Michaels, A.F., Knap, A.H., 1998. Influence of mesoscale eddies on new production in the Sargasso Sea. *Nature* 394, 263–266.
- Mulhearn, P.J., Filloux, J.H., Lilley, F.E.M., Bindoff, N.L., Ferguson, I.J., 1988. Comparisons between surface, barotropic and Abyssal flows during the passage of a warm-core ring. *Australian Journal of Marine and Freshwater Research* 39, 697–707.
- Murphy, A.H., 1988. Skill scores based on mean square error and their relationship to the correlation coefficient. *Monthly Weather Review* 116, 2417–2424.
- Nilsson, C.S., Cresswell, G.R., 1980. The formation and evolution of East Australian Current warm-core eddies. *Progress in Oceanography* 9, 133–183.
- Oey, L., 1988. A model of Gulf Stream frontal instabilities, meanders and eddies along the continental slope. *Journal of Physical Oceanography* 18 (2), 211–229.
- Oke, P.R., Middleton, J.H., 2000. Topographically induced upwelling off Eastern Australia. *Journal of Physical Oceanography* 30, 512–531.
- Oke, P.R., Allen, J.S., Miller, R.N., Egbert, G.D., Austin, J.A., Barth, J.A., Boyd, T., Kosro, P.M., Levine, M.D., 2002. A modeling study of the three-dimensional continental shelf circulation off Oregon: part I. Model-data comparisons. *Journal of Physical Oceanography* 32, 1360–1382.
- Oke, P.R., Schiller, A., Griffin, G.A., Brassington, G.B., 2005. Ensemble data assimilation for an eddy-resolving ocean model. *Quarterly Journal of the Royal Meteorological Society* 131, 3301–3311.
- Oke, P.R., Schiller, A., 2007. Impact of Argo. SST and altimeter data on an eddy-resolving ocean reanalysis. *Geophysical Research Letters* 34, L19601. doi:10.1029/2007GL031549.
- Oke, P.R., Brassington, G.B., Griffin, D.A., Schiller, A., 2008. The bluelink ocean data assimilation system (BODAS). *Ocean Modelling* 21, 46–70. doi:10.1016/j.jocmod.2007.11.002.
- Oke, P.R., Brassington, G.B., Griffin, D.A., Schiller, A., 2009. Data assimilation in the Australian bluelink system. *Mercator Newsletter* 34, 35–44.
- Osgood, K.E., Bane Jr., J.M., Dewar, W.K., 1987. Vertical velocities and dynamical balances in Gulf stream meanders. *Journal of Geophysical Research* 92 (C12), 13029–13040.
- Penven, P., Lutjeharms, J.R.E., Marchesiello, P., Roy, C., Weeks, S.J., 2001. Generation of cyclonic eddies by the Agulhas current in the lee of the Agulhas bank. *Geophysical Research Letters* 27, 1055–1058.
- Ridgway, K.R., Dunn, J.R., Wilkins, J.L., 2002. Ocean interpolation by four-dimensional weighted least squares: Application to the waters around Australasia. *Journal of Atmospheric and Oceanic Technology* 19, 1357–1375.
- Ridgway, K.R., Dunn, J.R., 2003. Mesoscale structure of the mean East Australian current system and its relationship with topography. *Progress in Oceanography* 56, 189–222.
- Roemmich, D., Gilson, J., 2001. Eddy transport of heat and thermocline waters in the North Pacific: A key to interannual/decadal climate variability? *Journal of Physical Oceanography* 31 675–687.
- Roughan, M., Middleton, J.H., 2002. A comparison of observed upwelling mechanisms off the east coast of Australia. *Continental Shelf Research* 22, 2551–2572.
- Schiller, A., Oke, P.R., Brassington, G.B., Entel, M., Fiedler, R., Griffin, D.A., Mansbridge, J.V., 2008. Eddy-resolving ocean circulation in the Asian-Australian region inferred from an ocean reanalysis effort. *Progress in Oceanography* 76, 334–365.
- Schiller, A., Ridgway, K.R., Steinberg, C.R., Oke, P.R., 2009. Dynamics of three anomalous SST events in the Coral Sea. *Geophysical Research Letters* 36, L06606. doi:10.1029/2008GL036997.
- Schiller, A., Wijffels, S.E., Sprintall, J., Molcard, R., Oke, P.R., 2010. Pathways of intraseasonal variability in the Indonesian throughflow region. *Dynamics of Atmospheres and Oceans* 50, 174–200. doi:10.1016/j.dynatmoce.2010.02.003.
- Singer, J.J., Atkinson, L.P., Blanton, J.O., Yoder, J.A., 1983. Cape Romain and the Charleston bump: historical and recent hydrographic observations. *Journal of Geophysical Research* 88 (C8), 4685–4698.
- Thompson, P.A., Baird, M.E., Ingleton, T., Doblin, M.A., 2009. Long-term changes in temperate Australian coastal waters and implications for phytoplankton. *Marine Ecology Progress Series* 384, 1–19.
- Tranter, et al., 1986. The coastal enrichment effect of the East Australian Current eddy field. *Deep-Sea Research* 33, 1705–1721.
- Wilkin, J.L., Zhang, W.G., 2007. Modes of mesoscale sea surface height and temperature variability in the East Australian Current. *Journal of Geophysical Research* 112, C01013. doi:10.1029/2006JC003590.